Doctor of Philosophy

Dispersion characteristics and leakage localization experimental study of ultrasonic guided waves in steel pipes

The Graduate School

of the University of Ulsan

Department of Mechanical and Automotive Engineering

Qi Wu

Dispersion Characteristics and Leakage Localization Experimental Study of Ultrasonic Guided Waves in Pipes

Supervisor: Professor Chang-Myung Lee

Author: Qi Wu

Department of Mechanical and Automotive Engineering
University of Ulsan

A dissertation submitted to the faculty of the University of Ulsan in partial fulfillment the requirement for the degree of Doctor of Philosophy in the Department of Mechanical and Automotive Engineering.

Ulsan, Korea

June 3th, 2019

Approved by

_____

Professor Chang-Myung Lee

Qi Wu 의 공학박사학위 논문을 인준함

심사위원장	김도중	(인)
심사위원	박성태	(인)
심사위원	이병룡	(인)
심사위원	전두환	(인)
심사위원	이장명	(인)

울산대학교 대학원

2019 년 6 월

ABSTRACT

Dispersion Characteristics and Leakage Localization Experimental Study of Ultrasonic Guided Waves in Pipes

Qi Wu
Department of Mechanical and Automotive Engineering
The Graduate School
University of Ulsan

Leak detection and location in a gas distribution network are significant issues. The acoustic emission (AE) technique can be used to locate a pipeline leak. Firstly, this paper introduces the basic concepts of guided waves and proposes the derivation of the three-dimensional displacement vector and the group velocity dispersion curve of the guided wave in a pipe. Then the influence of the wall thickness and diameter on the dispersion curve of guided wave in a pipe is proposed.

The location error of the leak detection method depends on three parameters. They are the distance between two sensors, estimation of the time delay between two measured signals and the propagation velocity of leak-induced signals in the pipe. To decrease the error of leak location, some methods to determine the time delay and the wave velocity are proposed. To reduce the effects of noise on the time delay estimation, two kinds of filters are introduced, which are wavelet decomposition and empirical mode decomposition. Then a new leakage location method using the modified generalized cross-correlation (GCC) location method in combination with the attenuation-based location method using multilayer perceptron neural networks (MLPNN) is proposed. The GCC location method can compensate for the weakening

effect of the different propagation paths on the leakage-induced signals, it also can increase the degree of the correlation between two measured signals and improve the accuracy of the time delay estimation. Besides, the wave speed was determined more accurately by using the peak frequency in combination with the group speed dispersive curve of the fundamental flexural mode. The MLPNN locator was experimentally verified by using a pressurized piping system and a signal acquisition system. The average of the relative location errors obtained by the MLPNN locator was reduced by 14% compared to that using the cross-correlation (CCF) location method. Hence, the MLPNN locator is more suitable for locating a leak in a gas pipe than the CCF location method is.

ACKNOWLEDGMENTS

First, I would like to express my sincere gratitude to Prof. Chang-Myung Lee, my supervisor, for his invaluable guidance, encouragement, and living supporting during my Ph.D. program. Sincere gratitude is also expressed to the members of the advisory committee in the graduate school of the University of Ulsan, who are Prof. Kyoung Kwan Ahn, Prof. Young Jin Yum, and Prof. Jungsoo Ryue and the other professors who had taught me and helped me in the fields of system control theory, composite materials, acoustics and vibration.

Specifically, I wish to thank Prof. Hui He and associate Prof. Xiao-zhen Qu, the supervisors of my M.D. program in the Liaoning University of Technology, for their encouragement, guidance and help during the period of the graduate study. I wish to express my thanks to senior brothers Zhen-Hua Xu, Zhi Qiu, and Cong-hao Liu, for their recommendations, encouragements and help during my study in Korea.

My thanks are extended to the members in the Sound and Vibration laboratory of the University of Ulsan, especially to Huan-Yu Dong, Peng Wang, Guang-quan Hou, Min Chen and Hang Su for their advice on this manuscript and the help of life in Korea. I would like to thank the members of the SCIEN company, who are Woo-Jin Kim, Chae-Rok Lim, and Young-Wook Bae, for their guidance and help for experiments implementation during my Ph.D. program. Same thanks are also regarded to my friends, Ya-Li Yang, Jing Liu, Jin-Cheng Wang, Ji Liu, Tian-Jun Zhou, Ying-Xiao Yu, etc., for their help in my daily life.

Finally, I would like to express my sincere gratitude to my parents and my girlfriend for their understanding and encouragement.

CONTENTS

LIST OF FIGURES

LIST OF TABLES

ABBREVIATIONS

AE	Acoustic emission
CSD	Cross-spectral density
CCC	Cross-correlation coefficient
CCF	Cross-correlation function
CSD	Cross-spectral density
CWT	Continuous wavelet transform
DFT	Discrete Fourier transforms
DWT	Discrete wavelet transform
EMD	Empirical mode decomposition
FFT	Fast Fourier transform
GCC	Generalized cross-correlation function
IDFT	Inverse discrete Fourier transform
IFT	Inverse Fourier transform
IMF	Intrinsic mode functions
LE	Lower envelopes
ML	Maximum likelihood estimator
MLPNN	Multilayer perceptron neural networks
MSE	Mean squared error
PHAT	Phase transform
UE	Upper envelopes
SCOT	Smoothed coherence transforms
SNR	Signal-to-noise ratio

NOMENCLATURES

Δt	Time delay between two measured signals
l	Distance between two sensors
a	Inner radius of the pipe
h	Thickness of the pipe
x	Distance between the leak and one sensor
Z	Acoustic impedance
v	Wave propagation speed
V	Particle motion Speed
p	Sound pressure
ω	Angular frequency
k	Wave number
k_R	Real components of the wavenumber k
k_I	Imaginary components of the wavenumber k
ρ	Material Density
$\rho(\triangle t)$	Cross-correlation coefficient
c_L	Longitudinal wave velocity
c_p	*P*hase velocity
c_g	Group velocity
c_s	Shear wave velocity
$L(0,m)$	Longitudinal mode
$T(0,m)$	Torsional mode
$F(n,m)$	Flexural mode
m	Radial modal parameters

n	Circumferential modal parameters
u	Three-dimensional displacement vector
u_r	Radial displacement components
u_θ	Circumferential displacement components
u_z	Axial displacement components
λ , μ	Lame's constants
∇^2	Three dimensional Laplace operator
$\varnothing$	Compressional scalar potential function
H	Equal-capacity vector potential function
$F(r, t)$	Function of coordinate vector r and time t
$\Omega_{n,x}$	Differential operator
SV	Vertical deformation component of shear deformation
SH	Horizontal deformation component of shear deformation
L	Longitudinal deformation component
ε	*S*train
σ	Stress
η	Material loss factor
$H(\omega, l)$	Transfer function of two vibration signals
α	Attenuation factor
$s(t)$	Leakage-induced signals at the leak source
$n(t)$	Background noise
l_{est}	Distance estimation between the leak and one sensor
f_s	Sampling frequency
τ_{max}	*M*aximum time delay

N	Length of the Fourier transform
$\Psi_g(\omega)$	Generalized cross-correlation weighting estimator
$\Psi_s(\omega)$	Frequency weighting function of the SCOT estimator
$\Psi_P(\omega)$	Frequency weighting function of the PHAT estimator
$\Psi_M(\omega)$	Frequency weighting function of the ML estimator
$S_{x1x2}(\omega)$	Cross-spectral density of signals x_1 *and* x_2
$\gamma_{x1x2}(\omega)$	Coherence estimate of signals
$\delta(t)$	Dirac delta function
T	Observation time
E	Elastic modulus
I_n , K_n	Complex Bessel function
Z_n , W_n	Real Bessel function

Chapter 1 Introduction

1.1 Research background

Pipelines are used extensively to transport and distribute natural gas and other easy-flowing products, but it doesn't mean they are risk-free. Pipeline leakage is a common phenomenon in the continuous transportation process due to the corrosion of pipe walls [1], third-party interference [2], aging of the pipes [3], construction defects, ground movement and other reasons. Leakage may cause environmental pollution, energy loss, injuries, and even fatalities. Therefore, assuring the reliability of the pipeline infrastructure has become a critical need for the energy sector, and leakage location is one of the paramount concerns of pipeline operators and researchers. Leakage in high-pressure vessels generates stress waves, which propagates through the pipe wall and is measured by a vibration sensor mounted on the pipe wall.

Pipeline leakage detection methods include direct and indirect methods [4]. Direct methods detect the leaked product outside the pipeline using fiber optic sensing, moisture measurements, gas tracing, vapor sensing, etc. [5]; however, the sensitivities of these methods are low, and the corresponding sensors are expensive. The indirect methods detect leakage by measuring gas pressure, flow, temperature, etc. These parameters only can be measured by the sensors mounted inside the pipeline, but many pressurizing vessels in the industry are inaccessible, a nondestructive testing technique is necessary in these cases. Acoustic emission (AE) [6] is a nondestructive testing technique. Leakage in high-pressure systems can be detected and located by techniques based on AE theory. This technique provides quick leak detection, high sensitivity, accurate leak location, the ability to locate the spots of small-scale leaks [7], and low

false alarm rate comparing to conventional methods. The main disadvantage of this method is the inability to inspect long pipeline sections due to the low energy of AE signals. Therefore, it becomes a common leak location method now. AE is the radiation phenomenon of elastic waves in solids that occurs when a material has irreversible changes in its internal structure, for example as a result of crack formation or plastic deformation due to aging, temperature gradients or external mechanical forces. When a leak occurs, an air-structure coupling between the escaping gas and the pipe wall is formed, thus resulting in a stress wave that propagates along the body of the pipeline on both sides of the leak. This phenomenon, regarded as general acoustic emission, is referred to as stress wave emission and can be used to develop a dynamic nondestructive testing method for detecting and locating pipeline leaks. In this study, the AE signals in the pipe wall are detected by AE sensors mounted on the pipe's exterior surface.

Leakage location commonly relies on attenuation-based methods or time-of-flight-based methods [8]. The former methods are based on the reduction in the AE signal strength as the propagation distance increases. The prerequisite for the latter methods is that the wave speed is a known constant; however, the wave speed varies as a function of frequency due to the group speed dispersion nature of gas-leakage-induced guided waves [9]. To determine the speed of the AE signal, Li et al. [10] derived the wavenumber formulae to predict the wave speeds and thereby halved the location error compared to that using the theoretical wave speed. Davoodi and Mostafapour [11] derived the motion equation of the pipe for the simply supported boundary condition by the standard form of Donnell's nonlinear cylindrical shell theory. Nishino et al. [12] generated wide-band cylindrical waves in aluminum pipes by the laser-ultrasonic method; the experimental results showed good agreement between the theoretical and experimental group speed dispersion curves. In this study, the group speed of the leakage-induced signal is estimated by its peak frequency in combination with the group speed dispersive curve of the fundamental flexural mode.

When leakage-induced signals transmit along the pipe wall, signal distortion arises due to energy attenuation, dispersion effect [13] and reverberation. The cross-correlation function (CCF) can determine the time delay based on the similarity of two signals. However, due to the signal distortion of AE wave propagating in the pipeline, the cross-correlation analysis perform badly. To improve the leakage location accuracy, Davoodi and Mostafapour [14, 15] located a leak on a high-pressure gas pipe by wavelet transform, filtering technique, and CCF. Yu et al. [16] located the leakage by dual-tree complex wavelet transform and singular value decomposition. Brennan et al. [17] estimated the time delay between two channels by the time and frequency domain methods, with almost identical test results being obtained. Sun et al. [18] proposed a leakage aperture recognition and location method using the root mean square entropy of local mean deposition and Wigner-Ville time-frequency analysis. Guo et al. [19] proposed an adaptive noise cancellation method using the empirical mode decomposition, the test result showed that the time delay estimation of the leakage-induced signal is more accurate. Yang et al. [20] estimated the characteristics related to the two propagation channels by blind system identification. The travel duration of the leakage source signals from the leak point to either sensor was extracted from the identified propagation channel.

1.2 Review of leakage detection and localization

The pipeline leak detection technology is a combination of multi-disciplinary, various direct and indirect detection methods can be used. Direct leak detection methods include leak detection method using the cable, leak detection method using the

fiber sensor, etc [21]. Indirect leak detection methods include acoustic wave method, negative pressure wave method, mass/volume balance method and transient model method [22]. Some people also divide the leak detection technology into hardware-based methods and software-based methods as shown in Table 1.1 [23].

Table 1.1 Leakage detection methods.

Methods based on hardware	Acoustic detection methods	Listening rod, Leak correlator, Leak noise loggers, etc
	Non-acoustic detection methods	Gas injection, Ground penetrating radar technology, Infrared photography, etc
Methods based on software	Numerical modeling methods	Methods based on transient events: ITA, TDA, FDA, Traditional hydraulic model, etc
	Non-Numerical modeling methods	An artificial neural network, Bayesian inference system, Golden section method, adaptive Kalman

1.2.1 Leak detection method using the cable

Cable leak detection is commonly used to detect liquid hydrocarbon [24]. After the leaking material seeps into the cable, the characteristics of the cable will change. So the cable can be used to detect a leak in pipes. The following cables have been developed:

(1) Oil-soluble cable

There is a layer of the conductive film in the cable, it will dissolve and lose electrical conductivity when it touches hydrocarbons. After a pulse signal is sent from

one end of the cable, the circuit will cut off if the conductive film dissolve, the location of a leak can be detected based on the time delay of the reflective signal [25].

There are two parallel wires in another kind of the cable, the wires are covered with a layer of insulated oil-soluble film. After the oil penetrates the cable, a short circuit occurs between two wires. The leak location can be determined by measuring the resistance between the two wires.

(2) Permeable cable

The impedance of the cable will change when the oil penetrates the cable [26]. After an electrical pulse signal is sent from one end of the cable, a leak can be located by the impedance difference based on the reflected electrical signal.

(3) Distributed sensing cable

This kind of the cable is commonly used for hydrocarbon leak detection, such as kerosene solvent. The leak can be located by measuring the resistance of the wire loop. The sensing cables can also be connected to detect the leakage in long-distance pipelines.

1.2.2 Leak detection method using the fiber sensor

(1) Leak detection method using the distributed fiber sensor [27]

The probe of the sensor consists of a prism and an optical transceiver device. When the bottom surface of the prism is in contact with different media, the transmission loss of light in the prism is different, whether the pipe leaks can be detected based on the light intensity measured by the fiber sensor [28]. The disadvantage of this kind of sensor is that when the medium can’t be in contact with the prism, the pipeline leaks can’t be

detected.

(2) Multi-fiber probe telemetry

The optical fiber cladding can selectively adsorb hydrocarbons and change its refractive index, then the intensity of light in the optical fiber will change. The photoelectric conversion device in the probe can convert the optical signal into an electrical signal, and the leakage can be determined by detecting the intensity of the light signal.

(3) Fiber temperature sensor leak detection

Leakage of heated gas, viscous oils, crude oil and other heated substances can increase the temperature of the surrounding environment. The fiber optic temperature sensor can continuously measure the temperature along the pipe [29]. When the temperature exceeds the limit, the leakage in pipes can be detected. However, the sensors are expensive, which results in this method not being used commonly.

1.2.3 Mass and volume balance method

This method is based on the mass and volume balance of the fluid in the pipeline [30]. If the incoming flow rate is greater than the outgoing flow rate, it can be judged that there is a leak between two sensors. The detection accuracy of this method is subject to the flow meter. It is necessary to calculate the effect of a temperature drop on fluid density for pipe leak detection [31].

1.2.4 Acoustic wave method

Due to the pressure difference between the inside and outside of the pipe, the leaking gas forms a vortex when it reaches the outside of the pipeline through the leak

orifice [32]. Only the signals that resonate with the pipe can travel a long distance due to the damping effect of the pipe. Pipe wall vibrations caused by gas leakage include lateral vibration, longitudinal vibration and ring vibration [33]. Leak-induced signal can be detected and located by the acceleration sensor mounted on the pipe wall. Since the strength of the AE signals is affected by the damping effect of the pipe [34], the distance that can be detected is limited, and there is much noise in the city, which limits the application of this location methods. So many sensors should be installed to detect leaks over long distances. The energy attenuation in a buried pipe is more obvious, so this method is not suitable for detecting a leak in buried pipelines.

1.2.5 Negative pressure wave method

The gas pressure will suddenly drop when there is a leak in a pipe. The gas pressure drops caused by the leak will propagate to upstream and downstream of the pipe, which is called the negative pressure wave [35]. Since the attenuation of the negative pressure wave is small, the pressure drop signal can spread a long distance. The propagation speed of negative pressure wave can be considered as the sound waves speed in the fluid. The negative pressure wave can be located by the time delay between two signals measured in upstream and downstream and the propagation speed of the negative pressure wave in the pipe [36]. The leak can be located as the following equation

$$x = \frac{l + v\Delta t}{2}, \qquad (1.1)$$

where $\triangle t$ is the time delay between two signals measured in upstream and downstream, l is the distance between two sensors mounted in upstream and downstream measurement points, v is the propagation speed of negative pressure wave, x is the distance between the leak and one sensor

Based on the characteristics of the negative pressure wave, this method only can detect the leak just happened. In addition, the pressure sensor installed outside the station is difficult to maintain and easily damaged, so there are certain limitations for this method.

1.2.6 Transient model method

Transient models are built by conservation of mass, conservation of momentum, conservation of energy and the equation of state for the fluid [37]. Therefore, measurement values of flow, pressure and temperature are needed for leakage detection. A leak can be detected by the difference between the measured value and the predicted value of the flow.

This method can detect small leaks, but data acquisition equipment is expensive as many instrumentations are needed to collect data in real-time. The models employed are complex and they require a trained user.

1.3 Metrics for leak detection methods

The evaluation of the performance of the leak detection method should be considered from the following aspects:

(1) Sensitivity

The smallest amount of leakage material quantities that the data acquisition equipment can detect.

(2) Accuracy

This covers the estimation of leak parameters such as leak flow, total lost volume

and leak location. These leak parameter estimates should be as accurate as possible [24].

(3) Detection time

The duration from the leakage time to the time that the leakage location system can detect a leak.

(4) Universality

Whether the leak detection method can be used under different conditions, for example, the pipe material or transport media is changed.

(5) Maintainability

Repairment can be performed simply and quickly for the operator when the system is running or fails.

(6) Price

The ratio of the cost of system construction, operation and maintenance to the economic benefits that the system can provide.

There is no universal method due to the complexity of detection, such as the diversity of the transport medium in the pipe, the diversity of the environment (such as above ground, trenches, buried land, seabed), and the diversity of leakage forms (leakage, perforation, fracture, etc.). A leak detection method or a leak detection device can’t meet all requirements at the same time, therefore, several methods should be combined.

1.4 Research status of AE technology

1.4.1 AE technology features

AE is the radiation phenomenon of elastic waves in solids that occurs when a material has irreversible changes in its internal structure [38], for example, crack formation or plastic deformation due to aging, temperature gradients or external mechanical forces. Now the meaning of AE has been generalized, which can be the signals generated by leakage, friction and impact [39].

The application range of AE technology covers the fields of aviation, aerospace, petroleum, petrochemical, railway, automobile, construction, electric force and so on. The main objectives of AE detection include four aspects:

(1) Locate the AE source,

(2) Analyze the properties of the AE source,

(3) Determine the time or load of the AE source,

(4) Assess the severity of the AE source.

1.4.2 AE detection principle

The elastic wave emitted from the AE source to the surface of the medium [41]. The transient displacement of the medium surface is converted into an electrical signal by the AE sensor [42]. After the AE signal is amplified and processed, its characteristic parameters can be recorded and displayed. Finally, the characteristics of the AE source can be evaluated by the interpretation of the data.

1.5 Main contents and organization of this dissertation

The proposed method can be applicable for pipes with variable operating pressure, this study only deals with the location of a single leak source. The rest of this paper is organized as follows.

Chapter 2 introduces the basic concepts of acoustic impedance, phase velocity and group velocity of guided waves, proposes the derivation of the three-dimensional displacement vector, derives the group velocity dispersion curve of the guided wave in a pipe based on the Navier displacement motion equation. This chapter also proposes the influence of the wall thickness and diameter on the group velocity dispersion curves of the guided wave in a pipe.

Chapter 3 introduces the cross-correlation method for leak detection. The calculation of the CCF in the time domain and frequency domain are presented. This chapter also proposes the PHAT, SCOT and ML estimators with the desirable feature of sharpening the peak in the CCF.

Chapter 4 introduces some methods to determine the AE signal speed, such as the analytical method, time-of-flight method, cross-correlation method, three sensors methods and phase-frequency method. These methods don’t consider the dispersion characteristics of the AE signal, therefore, a new method based on the dispersion characteristics of the AE signal is proposed in this chapter.

Chapter 5 introduced two kinds of filters, which are wavelet decomposition and empirical mode decomposition, and the detailed steps of signal processing are proposed.

Chapter 6 proposed a leakage location method using the modified generalized cross-correlation (GCC) location method in combination with the attenuation-based

location method using multilayer perceptron neural networks (MLPNN). The modified GCC location method can compensate for the weakening effect of the different propagation paths on the leakage-induced signals, it also can increase the degree of the correlation between two measured signals and improve the accuracy of the time delay estimation.

Chapter 7 analyzes the leak-induced signals measured in-situ in the time domain and frequency domain, analyzes the location results using the improved method and CCF location method, finally analyzes the reasons for the improved location accuracy.

Chapter 8 made a summary of this paper.

Chapter 2 Propagation characteristics of elastic waves on pipes

2.1 Acoustic impedance

The basic concepts of acoustic impedance [43], phase velocity, group velocity and acoustic attenuation are the basis for understanding the propagation of guided waves in a pipe.

When elastic waves propagate in the medium, the ratio of the sound pressure p at any point to the velocity V of the point is called the acoustic impedance, which is measures of the opposition that a system presents to the acoustic flow resulting from an acoustic pressure applied to the system, and it can be expressed as

$$Z = \frac{p}{V}. \qquad (2.1)$$

The acoustic impedance is also equal to the product of density and sound velocity [44], i.e, $Z=\rho v$. Different media have different acoustic impedance; even in the same medium, the acoustic impedance is different for waves of different types. The acoustic impedance of gas, liquid and metal varies greatly, and the ratio of acoustic impedance between them is close to 1:3000:8000.

Acoustic impedance is an inherent constant of the material and can directly show the acoustic properties of the material [45]. When the ultrasonic wave encounters the interface between the two media, the acoustic impedance determines the energy ratio of reflection wave and transmission wave.

2.2 The basic concept of guided waves

Guided waves can be generated in plates, rods and pipes, which are called a

waveguide [46]. Phase velocity and group velocity are two important concepts in guided waves. The phase velocity of a wave is the rate at which the phase of the wave propagates in space, and the group velocity of a wave is the propagation velocity of the waveform [47], they are defined as

$$c_p = \frac{\omega}{k} \text{ and } c_g = \frac{\Delta\omega}{\Delta k}, \quad (2.2)$$

where c_p is the phase velocity, c_g is the group velocity, ω is the angular frequency, and $k=2\pi/\lambda$ is the wave number. The difference between phase velocity and group velocity can be written as

$$c_g = \frac{d(kc_p)}{dk} = c_p + k\frac{dc_p}{dk}. \quad (2.3)$$

Since $k=2\pi f/c_p$, the group speed can also be written as

$$c_g = c_p + f\frac{dc_p}{df}. \quad (2.4)$$

Therefore, the more intense the dispersion, the greater the difference between the phase velocity and the group velocity. The horizontal axis of the group velocity dispersion curve can be the product of the frequency and the thickness, then the group velocity can also be written as

$$c_g = \frac{c_p^2}{c_p - (fd)\frac{dc_p}{d(fd)}}. \quad (2.5)$$

2.3 The basic theory of guided wave in a pipe

The guided wave in the pipe is divided into longitudinal mode, torsional mode and flexural mode [48], respectively, which are denoted by *L(0,m)*, *T(0,m)* and *F(n,m)*,

respectively, where *n* and *m* represent the circumferential and radial modal parameters, respectively. The longitudinal mode and torsion mode are axisymmetric modes, and the flexural modes are non-axisymmetric modes.

The geometry of a cylindrical pipe is shown in Figure 2.1.

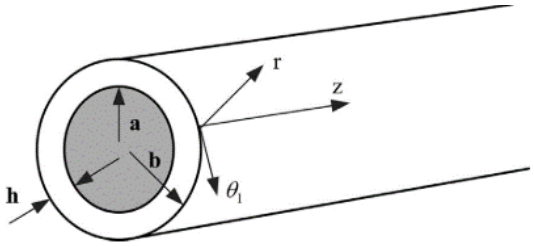

Figure 2.1 Schematic diagram of the pipe (*a* is inner radius, *b* is outer radius, *h* is the thickness of the pipe).

Considering the wave propagating in the infinite long pipe, the Navier displacement motion equation[49] should be satisfied, which is

$$\mu\nabla^2 u + (\lambda + 2\mu)\nabla\nabla \cdot u = \rho(\partial^2 u / \partial t^2), \qquad (2.6)$$

where u is the three-dimensional displacement vector, ρ is material density, λ and μ are Lame's constants, ∇^2 is the three dimensional Laplace operator. Based on the law of Helmholtz decomposition, the displacement vector can be decomposed into the compressional scalar potential function $\varnothing$ and the equal-capacity vector potential function H as

$$\begin{aligned} u &= \nabla\varphi + \nabla \times H, \\ \nabla \cdot H &= F(r,t), \end{aligned} \qquad (2.7)$$

where F is a function of coordinate vector r and time t. Substitution of Equation 2.7 into Equation 2.6 gives

$$c_L^2 \nabla^2 \varphi = \partial^2 \varphi / \partial t^2, \quad c_T^2 \nabla^2 H = \partial^2 H / \partial t^2. \tag{2.8}$$

The displacement equations of motion are satisfied if the potentials function $\varnothing$ and H satisfy the wave equations. The equation 2.8 describes the longitudinal waves and the shear waves, respectively. c_L and c_s are the longitudinal and shear wave velocities in the infinite isotropic medium, which are given as

$$c_L = \sqrt{\frac{\lambda + 2\mu}{\rho}} \text{ and } c_S = \sqrt{\frac{\mu}{\rho}}. \tag{2.9}$$

For the propagation of waves in a hollow cylinder, the potentials function $\varnothing$ and H can be described as

$$\begin{aligned} \varnothing &= f(r)\cos n\theta \cos(\omega t + kz), \\ H_r &= g_r(r)\sin n\theta \sin(\omega t + kz), \\ H_\theta &= g_\theta(r)\cos n\theta \sin(\omega t + kz), \\ H_z &= g_z(r)\sin n\theta \cos(\omega t + kz), \end{aligned} \tag{2.10}$$

where k is the component of the wave vector in the axial direction and n is the circumferential order. Since the differential operator is

$$\Omega_{n,x} = \left[\frac{\partial^2}{\partial x^2} + \frac{1}{x}\frac{\partial}{\partial x}\left(\frac{n^2}{x^2} - 1\right) \right], \tag{2.11}$$

then

$$\begin{aligned} &\Omega_{n,ar}[f] = 0, \\ &\Omega_{n,\beta r}[g_z] = 0, \\ &\Omega_{n+1,\beta r}[g_r - g_\theta] = 0, \\ &\Omega_{n-1,\beta r}[g_r + g_\theta] = 0, \end{aligned} \tag{2.12}$$

where $\alpha^2 = \omega^2 / c_L^2 - k^2$, $\beta^2 = \omega^2 / c_S^2 - k^2$. The general solution in Bessel form is

$$
\begin{aligned}
&f_1 = AZ_n(a_1 r) + BW_n(a_1 r),\\
&2g_1 = g_r - g_\theta = 2A_1 Z_{n+1}(\beta_1 r) + 2B_1 W_{n+1}(\beta_1 r),\\
&2g_2 = g_r + g_\theta = 2A_2 Z_{n-1}(\beta_1 r) + 2B_2 W_{n-1}(\beta_1 r),\\
&g_3 = A_3 Z_n(\beta_1 r) + B_3 W_n(\beta_1 r),
\end{aligned}
\qquad (2.13)
$$

where Z_n and W_n represent the Bessel function,

$$
a_1 r = |ar|, \beta_1 r = |\beta r|. \qquad (2.14)
$$

Assume g_r=-g_θ=g_1, the particle displacement can be expressed as:

$$
\begin{aligned}
u_r &= U_r(r)\cos n\theta \cos(\omega t + kz),\\
u_\theta &= U_\theta(r)\sin n\theta \cos(\omega t + kz),\\
u_z &= U_z(r)\cos n\theta \sin(\omega t + kz),
\end{aligned}
\qquad (2.15)
$$

where U_r, U_θ and U_z denote the radial, circumferential and axial displacement components, respectively. $u_r \neq 0$, $u_\theta = 0$ and $u_z \neq 0$ correspond to the longitudinal mode; $u_r = 0$, $u_\theta \neq 0$ and $u_z = 0$ correspond to the torsion mode: $u_r \neq 0$, $u_\theta \neq 0$ and $u_z \neq 0$ correspond to the flexural mode. Differentiation with respect to r yields the strain-displacement in cylindrical coordinates:

$$
\begin{aligned}
\varepsilon_{rr} &= \frac{\partial u_r}{\partial r},\\
\varepsilon_{r\theta} &= \frac{1}{2}\left[r\frac{\partial}{\partial r}\left(\frac{u_\theta}{r}\right) + \frac{1}{r}\frac{\partial u_r}{\partial \theta} \right],\\
\varepsilon_{rz} &= \frac{1}{2}\left[r\frac{\partial u_r}{\partial z} + \frac{1}{r}\frac{\partial u_z}{\partial \theta} \right].
\end{aligned}
\qquad (2.16)
$$

Hooke's law can be used to define relationships between stresses and strains [50]

$$
\begin{aligned}
\sigma_{rr} &= \Delta\lambda + 2\mu\varepsilon_{rr},\\
\sigma_{r\theta} &= 2\mu\varepsilon_{r\theta},\\
\sigma_{rz} &= 2\mu\varepsilon_{rz},
\end{aligned}
\qquad (2.17)
$$

where $\Delta = \nabla^2 \emptyset = -\left(\alpha^2 + k^2\right) f \cos(n\theta)\cos(\omega t + kz)$ is dilation. The boundary conditions for the pipe are given by

$$\sigma_{rr} = \sigma_{rz} = \sigma_{r\theta} = 0\,, (r = a, r = a + h = b)\,, \qquad (2.18)$$

having related strains to small displacements along the pipe, stresses are related to strains to yield the general form of Hooke's Law

$$\begin{bmatrix} \sigma_{rr} \\ \sigma_{\theta\theta} \\ \sigma_{zz} \\ \sigma_{\theta z} \\ \sigma_{rz} \\ \sigma_{r\theta} \end{bmatrix} = \begin{vmatrix} c_{11} & c_{12} & c_{13} & c_{14} & c_{15} & c_{16} \\ c_{21} & c_{22} & c_{23} & c_{24} & c_{25} & c_{26} \\ c_{31} & c_{32} & c_{33} & c_{34} & c_{35} & c_{36} \\ c_{41} & c_{42} & c_{43} & c_{44} & c_{45} & c_{46} \\ c_{51} & c_{52} & c_{53} & c_{54} & c_{55} & c_{56} \\ c_{61} & c_{62} & c_{63} & c_{64} & c_{65} & c_{66} \end{vmatrix} \times \begin{bmatrix} L^{+} \\ L^{-} \\ SV^{+} \\ SV^{-} \\ SH^{+} \\ SH^{-} \end{bmatrix}, \qquad (2.19)$$

where *SV* is the vertical deformation component of shear deformation, *SH* is the horizontal deformation component of shear deformation and *L* is the longitudinal deformation component. The positive and negative signs refer to the direction of propagation. The characteristic equation formed by the determinant of the Bessel functions is

$$\left|C_{ij}\right| = 0, \left(i,\, j = 1, 2, 3, \cdots 6\right), \qquad (2.20)$$

where *i* denotes the rows and *j* denotes the columns of the determinant. Hence, the dispersion characteristic equation for a hollow cylinder is given by

$$\left[C_{ij}\right] = \begin{vmatrix} c_{11} & c_{12} & c_{13} & c_{14} & c_{15} & c_{16} \\ c_{21} & c_{22} & c_{23} & c_{24} & c_{25} & c_{26} \\ c_{31} & c_{32} & c_{33} & c_{34} & c_{35} & c_{36} \\ c_{41} & c_{42} & c_{43} & c_{44} & c_{45} & c_{46} \\ c_{51} & c_{52} & c_{53} & c_{54} & c_{55} & c_{56} \\ c_{61} & c_{62} & c_{63} & c_{64} & c_{65} & c_{66} \end{vmatrix}, \qquad (2.21)$$

where

$$
\begin{aligned}
c_{11} &= \left[2n(n-1)-(\beta^2-\zeta^2)a^2\right]Z_n(a_1a)+2\lambda_1 a_1 a Z_{n+1}(a_1a),\\
c_{12} &= 2k\beta_1 a^2 Z_n(\beta_1 a)-2ka(n+1)Z_{n+1}(\beta_1 a),\\
c_{13} &= -2n(n-1)Z_n(\beta_1 a)+2\lambda_2 n\beta_1 a Z_{n+1}(\beta_1 a),\\
c_{14} &= \left[2n(n-1)-(\beta^2-k^2)a^2\right]W_n(a_1a)+2a_1 a W_{n+1}(a_1a),\\
c_{15} &= 2\lambda_2 k\beta_1 a^2 W_n(\beta_1 a)-2(n+1)kaW_{n+1}(\beta_1 a),\\
c_{16} &= -2n(n-1)W_n(\beta_1 a)+2n\beta_1 a W_{n+1}(\beta_1 a),\\
c_{21} &= 2n(n-1)Z_n(a_1a)-2\lambda_1 n a_1 a Z_{n+1}(a_1a),\\
c_{22} &= -k\beta_1 a^2 Z_n(\beta_1 a)+2ka(n+1)Z_{n+1}(\beta_1 a),\\
c_{23} &= -\left[2n(n-1)-\beta^2 a^2\right]Z_n(\beta_1 a)-2\lambda_2\beta_1 a Z_{n+1}(\beta_1 a),\\
c_{24} &= 2n(n-1)W_n(a_1a)-2na_1 a W_{n+1}(a_1a),\\
c_{25} &= -\lambda_2 k\beta_1 a^2 W_n(\beta_1 a)+2ka(n+1)W_{n+1}(\beta_1 a),\\
c_{26} &= -\left[2n(n-1)-\beta^2 a^2\right]W_n(\beta_1 a)-2\beta_1 a W_{n+1}(\beta_1 a),\\
c_{31} &= 2nkaZ_n(a_1a)-2\lambda_1 k a_1 a^2 Z_{n+1}(a_1a),\\
c_{32} &= n\beta_1 a Z_n(\beta_1 a)-(\beta^2-k^2)a^2 Z_{n+1}(\beta_1 a),\\
c_{33} &= -nkaZ_n(\beta_1 a),\\
c_{34} &= 2nkaW_n(a_1a)-2ka_1 a^2 W_{n+1}(a_1a),\\
c_{35} &= \lambda_2 n\beta_1 a W_n(\beta_1 a)-(\beta^2-k^2)a^2 W_{n+1}(\beta_1 a),\\
c_{36} &= -nkaW_n(\beta_1 a),
\end{aligned}
\qquad (2.22)
$$

where W_n and Z_n represent the Bessel functions with type depending on the value of n. Table 2.1 shows the appropriate selection of the Bessel functions for selected wave characteristics. As previously mentioned, n is the circumferential order of guided waves in a hollow cylinder. n is equal to zero when the modes are axially symmetric. It can change as θ varies but it remains axially symmetric. For axially symmetric modes the frequency equation can be decomposed into the product of two determinants as

$$D_1 \cdot D_2 = 0, \qquad (2.23)$$

where

$$D_1 = \begin{vmatrix} c_{11} & c_{12} & c_{14} & c_{15} \\ c_{31} & c_{32} & c_{34} & c_{35} \\ c_{41} & c_{42} & c_{44} & c_{45} \\ c_{61} & c_{62} & c_{64} & c_{65} \end{vmatrix}, D_2 = \begin{vmatrix} c_{23} & c_{26} \\ c_{53} & c_{56} \end{vmatrix}. \qquad (2.24)$$

$D_1=0$ and $D_2=0$ are the dispersion equations of longitudinal mode and torsional mode, respectively.

Table 2.1 Bessel function coefficients used for different values of the frequency range.

Wavenumber	Frequency range	Coefficient	Bessel Functions
Real	$\frac{\omega}{k} < C_l, C_s$	$\beta^2, \alpha^2 < 0,$ $\lambda_1 = \lambda_2 = -1$	$Z_n(\alpha r) = I_n(\alpha r)$ $W_n(\alpha r) = K_n(\alpha r)$ $Z_n(\beta r) = I_n(\beta r)$ $Z_n(\beta r) = K_n(\beta r)$
Real	$C_s < \frac{\omega}{k} < C_l$	$\alpha^2 < 0$ $\beta^2 > 0$ $\lambda_1 = -1$ $\lambda_2 = 1$	$Z_n(\alpha r) = I_n(\alpha r)$ $W_n(\alpha r) = K_n(\alpha r)$ $Z_n(\beta r) = I_n(\beta r)$ $Z_n(\beta r) = Y_n(\beta r)$
Real	$\frac{\omega}{k} > C_l, C_s$	$\beta^2, \alpha^2 > 0,$ $\lambda_1 = \lambda_2 = 1$	$Z_n(\alpha r) = I_n(\alpha r)$ $W_n(\alpha r) = K_n(\alpha r)$ $Z_n(\beta r) = I_n(\alpha r)$ $Z_n(\beta r) = K_n(\beta r)$
Imaginary	Any		
Complex	Any	β^2, α^2 Complex $\lambda_1 = \lambda_2 = 1$	

λ_1 and λ_2 are weighting coefficients,
I_n and K_n are complex Bessel functions,
J_n and Y_n are real Bessel functions.

2.4 Dispersion characteristics of guided wave in a pipe

Since the velocities of the elastic wave are different at different frequencies, which leads to the group speed dispersion of elastic waves [51]. This phenomenon will distort the elastic wave signal waveform during propagation, which makes it difficult to identify and extract the signal features [52]. Therefore, the most concerned problems are often the modal selection in the guided wave technology and the analysis of dispersion curves [53].

2.4.1 Dispersion curves of guided wave in a pipe

The dispersion curves of the guided wave in a pipe describe the relationship between phase velocity, group velocity, mode and frequency [54], which is determined by the material, diameter and wall thickness of the pipe. The phase and group velocity dispersion curve can be obtained by the MATLAB program. In this study, the pipe is made of steel, its inner diameter is 27.8 mm, the pipe wall thickness is 2.8 mm. Figure 2.2, Figure 2.3 and Figure 2.4 show the phase and group velocity dispersion curves of the torsional mode, longitudinal mode and flexural mode of the given pipe, respectively.

It's can be seen from figure 2.3 and 2.4, guided waves have the cutoff frequency, which can't propagate below the cutoff frequency [55]. The more the circumferential and radial modal parameters, the higher the cutoff frequency.

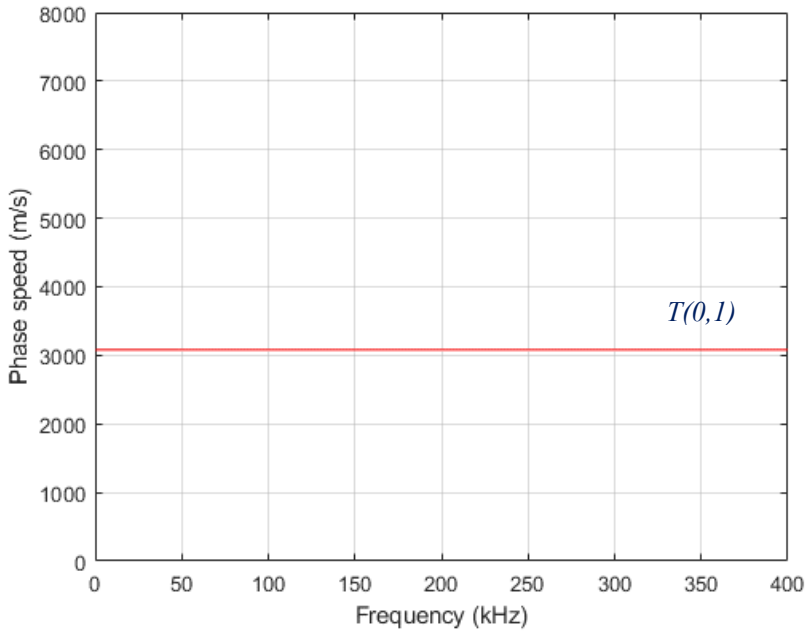

(a)

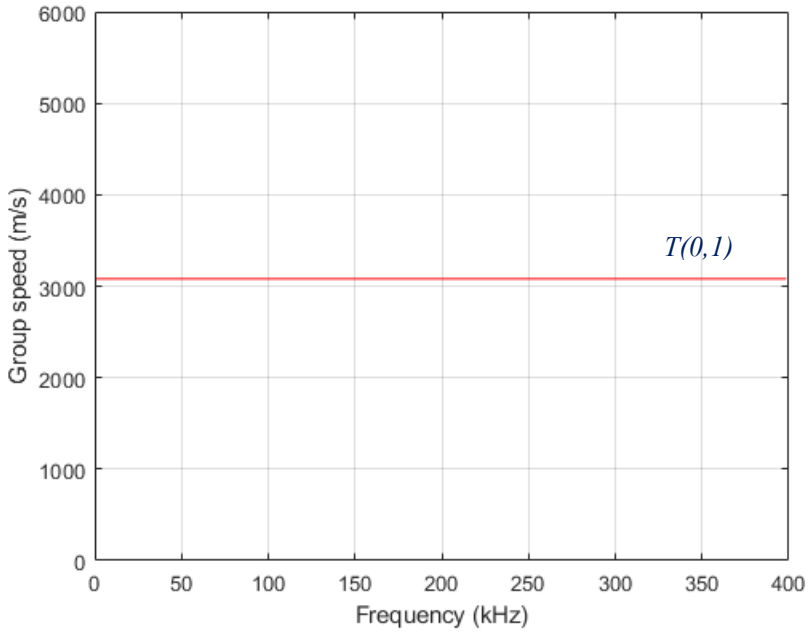

(b)

Figure 2.2 Dispersive curves of the torsional mode. (a) phase speed (b) group speed.

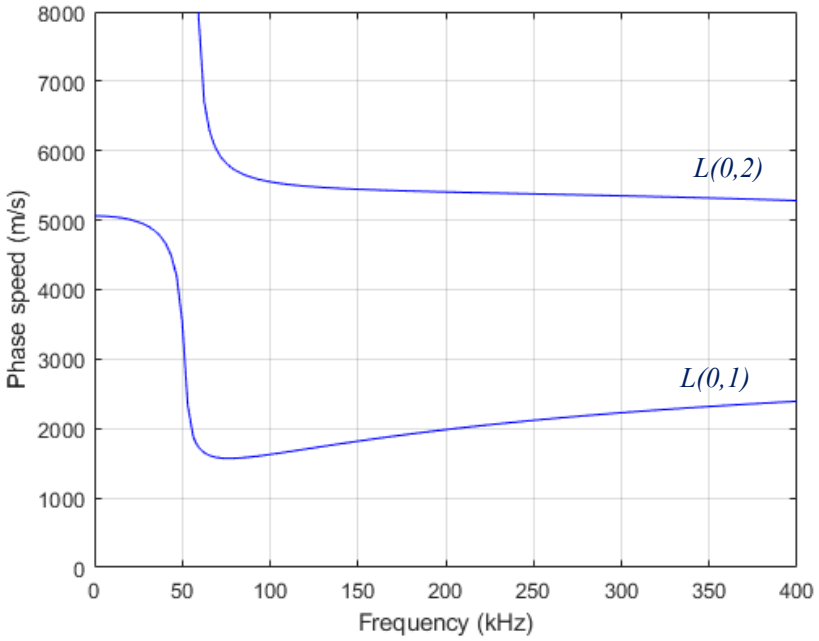

(a)

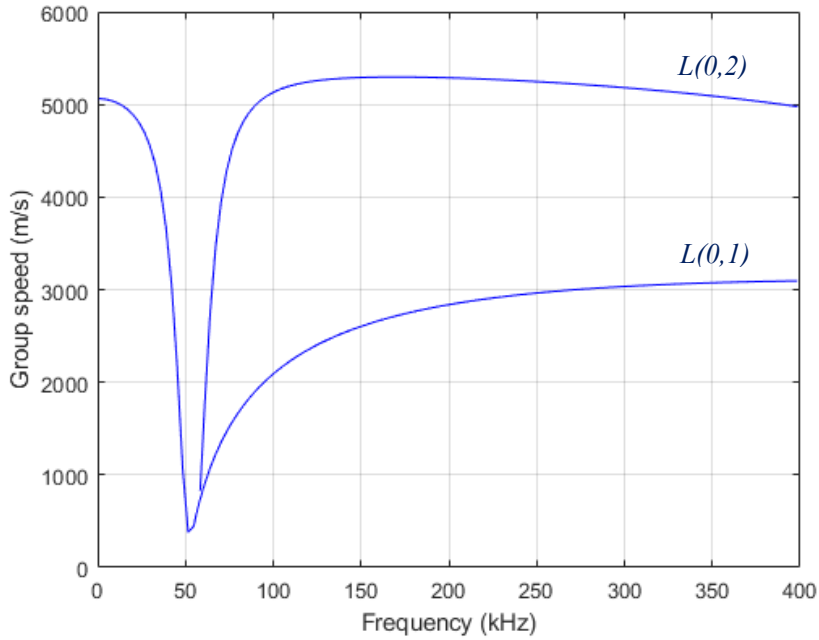

(b)

Figure 2.3 Dispersive curves of the longitudinal mode. (a) phase speed (b) group speed.

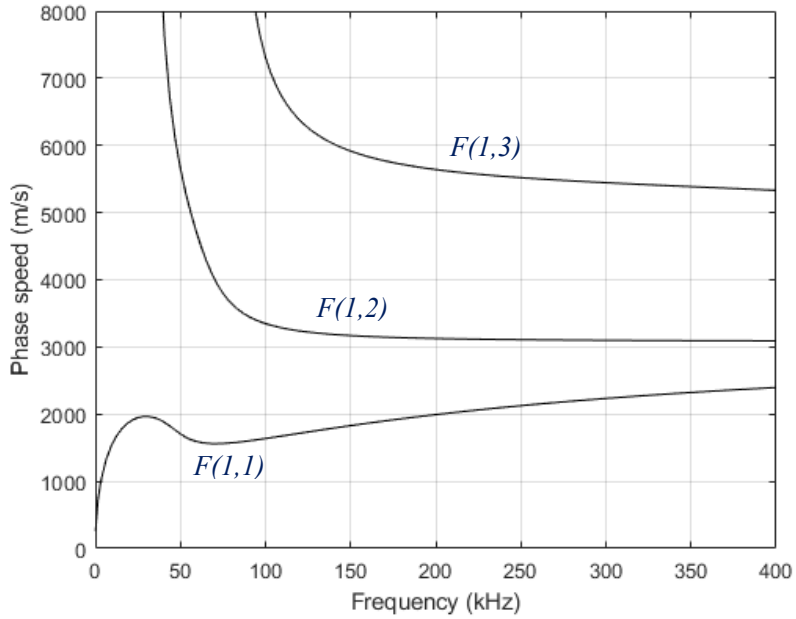

(a)

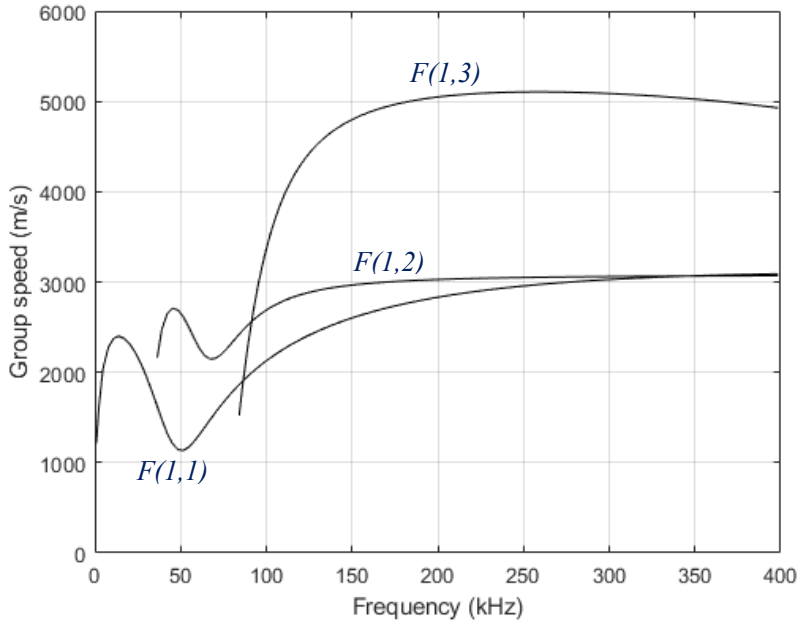

(b)

Figure 2.4 Dispersive curves of the flexural mode. (a) phase speed (b) group speed.

When the diameter of the pipe is larger enough than the wall thickness, the longitudinal modal guided wave in the pipe corresponds to the Lamb wave in the plate[56]. *L(0,1)* mode and *L(0,2)* mode correspond to the Lamb wave (A_0 mode) in the plate and the Lamb wave (S_0 mode), respectively [57]. *L(0,3)* mode and *L(0,4)* mode

are similar to the Lamb wave (A_1 mode) and symmetric Lamb wave (S_1 modal), respectively.

2.4.2 Influence of the wall thickness and diameter on the group speed dispersion curves of guided wave in a pipe

The group speed dispersion curves of the guided wave in the pipe can be determined by inner diameter, thickness, elastic modulus, Poisson's ratio and density of the pipe wall [58]. The influence of inner diameter a and wall thickness h on the group velocity dispersion curve is discussed below.

(1) h is fixed, a is variable at the same time.

Figure 2.5a is longitudinal modal group velocity dispersion curves with the same h but a is different. As can be seen from Figure 2.5a, the frequency at which the minimum longitudinal modal group velocity decreases as a decreases. The larger the frequency, the smaller the difference between the group velocities.

Figure 2.5b is torsional modal group velocity dispersion curves with the same h but a is different. For the torsional modal group velocity in Figure 2.5b, the dispersion curves coincide, so the change of the a has no effect on its dispersion characteristics.

Figure 2.5c is flexural modal group velocity dispersion curves with the same h but a is different. As can be seen from Figure 2.5c, the larger the frequency, the smaller the difference between the flexural modal group velocities.

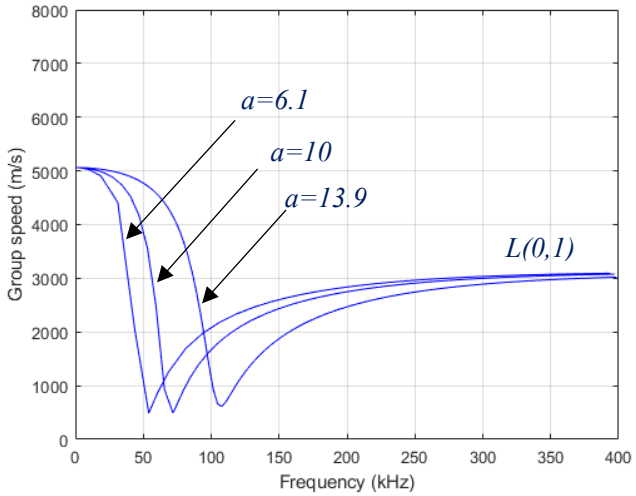

(a)

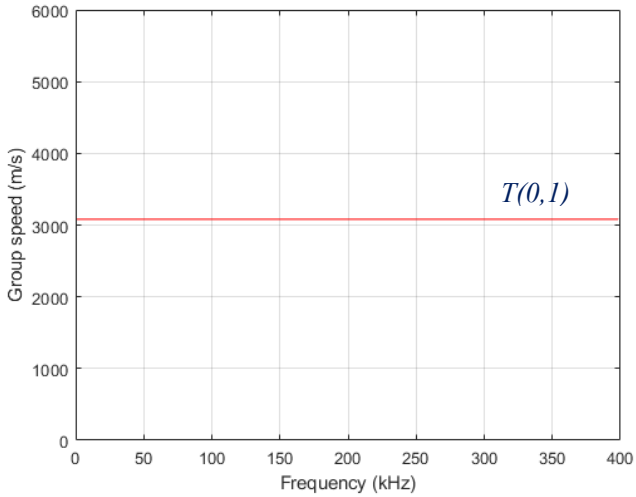

(b)

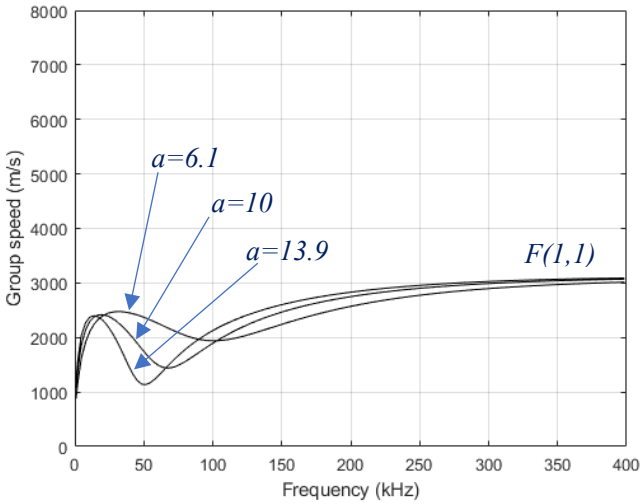

(c)

Figure 2.5 Group speed dispersion curves of three guided wave modes when h=2.8 and *a=6.1, 10 and 13.9* (a) longitudinal modal, (b) torsional modal, (c) flexural modal.

(2) *a* is fixed, *h* is variable at the same time.

Figure 2.6a is longitudinal modal group velocity dispersion curves with the same *a* but *h* is different. As can be seen from Figure 2.6a, the frequency at which the minimum longitudinal modal group velocity decreases as *a* decreases. The larger the frequency, the smaller the difference between the group velocities.

Figure 2.6b is torsional modal group velocity dispersion curves with the same *a* but *h* is different. For the torsional modal group velocity in Figure 2.6b, the dispersion curves coincide, so the change of the *h* has no effect on its dispersion characteristics.

Figure 2.6c is flexural modal group velocity dispersion curves with the same *a* but *h* is different. As can be seen from Figure 2.6c, the larger the frequency, the smaller the difference between the flexural modal group velocities.

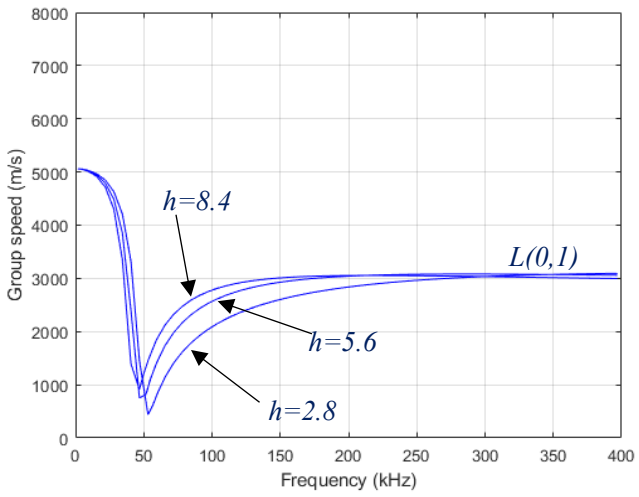

(a)

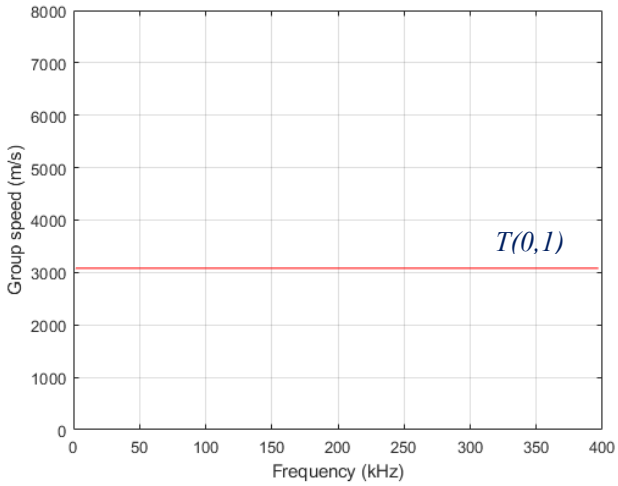

(b)

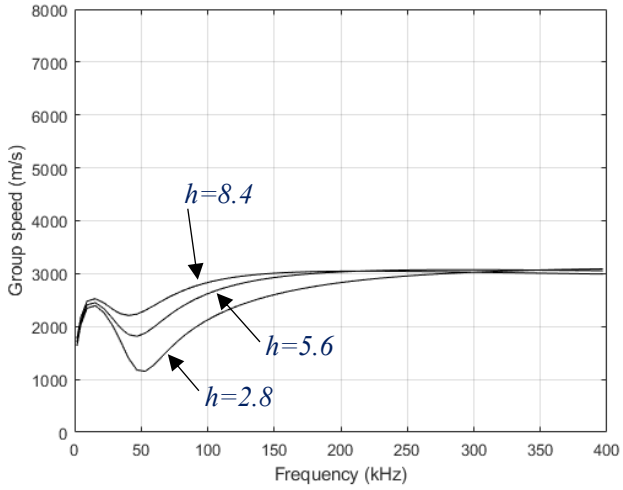

(c)

Figure 2.6 Group speed dispersion curves of three guided wave modes when a=13.9 and h=*2.8, 5.6 and 8.4* (a) longitudinal modal, (b) torsional modal, (c) flexural modal.

2.5 Wave attenuation

When elastic waves propagate in the medium, the energy of the wave decreases as the propagation distance increases, which is called the attenuation of elastic wave. According to different mechanisms of the wave attenuation, it can be divided into three types: diffusion attenuation, dispersion attenuation and absorption attenuation.

2.5.1 Diffusion attenuation

The cross-section area of the sound beam increases as the propagation distance increases, which is the sound beam diffusion. The vibration energy per unit area gradually decreases as the cross-section area of the sound beam increases, which is the diffusion attenuation [59]. The displacement *u(r)* of the particle on the surface of the spherical wave is inversely proportional to the distance *r* away from the vibration source.

$$u(r) \propto \frac{1}{r}. \qquad (2.25)$$

2.5.2 Structural scattering

Scattering attenuation is caused by the inhomogeneity of the vibration medium [60]. When the elastic wave propagates in the anisotropic material, there will be much reflection wave and refraction wave, which will lead to the reduction of the signal energy [61].

2.5.3 Energy absorption

Absorption attenuation is the phenomenon that the elastic wave energy is weakened by internal friction, heat conduction and dislocation movement in materials when the wave propagates in the medium [62]. In solid media, absorption tenuation is almost negligible relative to scattering attenuation. Amplitude attenuation caused absorption and scattering can be expressed by

$$u_a(r) = u_0 e^{-a_1 r}, \qquad (2.26)$$

where $u_a(r)$ is the amplitude of the peak value of the elastic wave at a distance away from vibration source; u_0 is the elastic wave peak amplitude at vibration source; a_1 is

an attenuation factor, which denotes the degree that elastic waves weaken with distance.

2.6 Theoretical analysis of the attenuation of leak-induced signals

Since diffusion attenuation, dispersion attenuation and absorption attenuation are coupled, attenuation measurements include the influence of all effects and it is often impossible to separate them. Therefore, a negative imaginary part is introduced in the wavenumber which quantifies the frequency dependent wave attenuation [65]. The sign is negative because the attenuation refers to the decrease in amplitude of the propagating wave with distance along the pipeline. The attenuation in the longitudinal direction can be calculated as the following equation

$$\alpha = -\frac{\mathrm{Im}\{k\}}{\omega} = \frac{k_f(\frac{B_f a\eta}{Eh})}{\omega\sqrt{1+\frac{2B_f a}{Eh}}} = \frac{1}{c_f}\frac{\frac{B_f a\eta}{Eh}}{\sqrt{1+\frac{2B_f a}{Eh}}}, \qquad (2.27)$$

where the attenuation factor α is inversely proportional to the wave speed and is dependent upon the radius a, wall thickness h, Young's Modulus E and material loss factor η of pipe. It is difficult to determine the dimensions of buried pipe, material loss factor and the number of discontinuities between two sensors, so it is not possible to accurately calculate the attenuation of leak-induced signals. Therefore, a new method is proposed in this section for the estimation of attenuation of leak-induced signals with distance along the pipe.

Implementation of the proposed method assumes that the attenuation can be calculated from the transfer function of the vibration measurements taken at two

positions along the pipeline. The attenuation of leak-induced signals can be expressed in terms of the ratio of transfer functions at two locations as

$$H(\omega,l) = H(\omega,x_1)/H(\omega,x_2) = \frac{e^{-j\omega\Delta x_1/c}e^{-\omega\alpha\Delta x_1}}{e^{-j\omega\Delta x_2/c}e^{-\omega\alpha\Delta x_2}} = e^{-j\omega l/c}e^{-\omega\alpha l}, \qquad (2.28)$$

where l is the distance between two sensors. Taking the magnitude and log to get the attenuation as

$$Attenuation(dB/m) = \frac{-20\ln|H(\omega,l)|}{l\ln 10}. \qquad (2.29)$$

Since the wavenumber k is related to the speed c and attenuation α of leak signals by

$$k = \frac{\omega}{c} - j\alpha\omega, \qquad (2.30)$$

where the attenuation α with distance is related to the imaginary part of the wavenumber. Substitution of Equation 2.32 into Equation 2.31 gives

$$Attenuation(dB/m) = \frac{-20\ln k}{l\ln 10} = 8.69\alpha\omega. \qquad (2.31)$$

Equating Equation 2.33 and 2.31 to have

$$\alpha = \frac{\ln|H(\omega,l)|}{\omega l}. \qquad (2.32)$$

Thus, the attenuation factor α can be calculated from the slope of the attenuation and frequency.

The energy of the AE signal reduces as the propagation distance increases due to geometric spreading, structural scattering, and energy absorption [14]. The weakening effect of the pipe on AE signals is similar to the low-pass filter [10], in that the cut-off frequency decreases as the propagation distance increases. When the AE signals propagate in one direction along the pipe wall, the energy attenuation of the AE signal

can be described by an exponential decay [63]

$$E = E_0 e^{-kl_i}, \quad (2.33)$$

where E is the energy of the measured signal, E_0 is the AE signal energy at the leak point and k is the attenuation coefficient. The AE signal energy is proportional to the integral of the square of the signal amplitude [64], and can be written as

$$E = \int_0^{\Delta T} v^2 dt, \quad (2.34)$$

where ΔT represents the length of sample time in seconds, and v represents the instantaneous signal amplitude in voltages. If the distance between the vibration source and the sensor is fixed, the weakening effect of the pipe on the AE signal will also be fixed, irrespective of any leakage-induced signals or impulse response signals. The closer the sensor is to the leak source, the greater the energy of the measured signals. Then the energy ratios of two measured signals will gradually increase or decrease as the distance between the vibration source and one sensor increases. Therefore, a leak in pipes can be located by the signal energy ratios without knowing the wave speed or the time delay estimation.

2.7 Conclusions

Guided waves will be generated in pipes due to the leakage on the pipe wall. The guided wave in the pipe is divided into longitudinal mode, torsional mode and flexural mode. The three-dimensional displacement vector and the group velocity dispersion curve of the guided wave in a pipe can be derived based on the Navier displacement motion equation and known boundary conditions for the given pipe, which is stated in this chapter. The influence of the wall thickness and diameter on the dispersion curve of the guided wave in a pipe is stated in this chapter. Finally, this chapter proposes the theory of attenuation of leak-induced signals.

Chapter 3 Cross-correlation method for leakage location

The CCF is an efficient technique to detect and locate a leak in pipes [66]. This chapter proposes the cross-correlation method and the three parameters affecting the leakage location accuracy, which are the distance between two sensors, velocity of the elastic wave and time delay estimation.

3.1 Introduction

A leak in pipes generates noise, whose characteristics depend primarily on gas jet velocity [10], pipe material, the size and shape of the leak orifice. The noise consists of acoustic noise and pipe wall vibrations. The pipe wall vibration signals travel along the pipe wall, which can be measured by the vibration sensors. The location accuracy relies on the wave speed estimation of leak-induced signals in the pipe and the time delay estimation between the two measured signals. The wave velocity can be estimated either by the theoretical methods based on pipe characteristics or by measuring on-site [67]. The time delay can be estimated by CCF. Various types of CCFs are discussed and compared in this chapter. The parameters on which CCFs depend are also discussed.

3.2 Cross-correlation method for leakage detection

The leak-induced signals generated at the leak source travel in both upward and downward directions through the pipe wall. These signals get attenuated along the pipe in both directions. While measuring leak-induced signals, the sensor also picks up the background noise. Thus, the measured signals can be written as

$$x_1(t) = s_1(t) + n_1(t),$$
$$x_2(t) = s_2(t) + n_2(t), \quad (3.1)$$

where $s_1(t)$ and $s_2(t)$ are the leakage-induced signals at the leak source, $n_1(t)$ and $n_2(t)$ represent the background noise measured by two sensors, respectively. The noise signals $n_1(t)$ and $n_2(t)$ are generated by the circuit components in the sensor and electromagnetic noises near the sensor. Three assumptions are listed below

(1) The signals $s_1(t)$, $s_2(t)$, $n_1(t)$ and $n_2(t)$ are stationary.

(2) The signals $s_1(t)$ and $s_2(t)$ are uncorrelated with noise signals $n_1(t)$ and $n_2(t)$.

(3) The noise signals $n_1(t)$ and $n_2(t)$ are uncorrelated with each other.

Cross-correlation method is the basic method for detecting and locating a leak, it can estimate the time delay between two signals measured on both sides of a leak. If there is a leak between the two sensors, the CCF will have a distinct peak[68]. The time delay can be calculated as the product between the sampling period and the shift of the CCF maximum peak [69]. Assuming the time delay between two measured signals as $\triangle t$, the leakage can be located by [70]

$$l_{est} = \frac{l + v(\omega_0)\Delta t}{2}, \quad (3.2)$$

where $v(\omega_0)$ is the propagation speed of leak-induced signals in pipes, l is the distance between the two sensors, l_{est} is the distance estimation between the leak and one sensor. From Equation 3.2, the location accuracy depends upon three factors:

(1) Distance between two sensors

This parameter can be measured onsite by measuring wheel or tape. However, it's

difficult to measure accurately in some situations, such as in the presence of unexpected loops or bends in buried pipes.

(2) Propagation speed

The propagation speed of leak-induced signals in pipes is a critical factor in locating a leak. In this study, the wave speed is online estimated by the peak frequency of the leak-induced signals in combination with the known group speed dispersive curve of the fundamental flexural mode [9].

(3) Time delay

The time delay is estimated by the CCF between two signals measured by the sensors. The quality of the time delay estimation depends upon the variance of the peak in the cross-correlation coefficient [71].

3.2.1 Cross-correlating continuous signals in the time domain

The CCF is given by

$$R_{x_1x_2}(\tau) = E\left[x_1(t)x_2(t+\triangle t)\right]. \qquad (3.3)$$

The shift of the maximum peak in the CCF provides the time delay estimation between the two measured signals[72], and *E[*]* denotes the expectation operator. The two signals $x_1(t)$ and $x_2(t)$ are measured for a fixed finite time interval, $0 \le t \le T$, thus the biased cross-correlation estimator $\hat{R}_{x_1x_2}$ is given by

$$\begin{aligned} \hat{R}_{x_1x_2}(\tau) &= \frac{1}{T}\int_0^{T-\tau} x_1(t)x_2(t+\Delta t)dt, \tau > 0, \\ \hat{R}_{x_1x_2}(\tau) &= \frac{1}{T}\int_{-\tau}^{T} x_1(t)x_2(t+\Delta t)dt, \tau < 0, \end{aligned} \qquad (3.4)$$

where $1/T$ refers to the normalization scale factor. Due to the noises and wave

attenuation, the measured signals may vary significantly with time, which results in fluctuations in the CCF. These fluctuations may be large, which makes it difficult to identify the peak in CCF. Therefore, it is advantageous to express the CCF in the cross-correlation coefficient [73], which is the dimensionless form of the CCF and written as

$$\rho(\Delta t) = \frac{\hat{R}_{x_1x_2}(\Delta t)}{\sqrt{\hat{R}_{x_1x_1}(0)\hat{R}_{x_2x_2}(0)}}, \qquad (3.5)$$

where $\hat{R}_{x_1x_1}(0)$ and $\hat{R}_{x_2x_2}(0)$ are amplitudes in the autocorrelation functions of $x_1(t)$ and $x_2(t)$ at $\Delta t=0$.

An example of a biased cross-correlation estimator is shown in Figure 3.1. Figure 3.1a shows an impulse response signal, Figure 3.1b shows the same signal delayed by 1 second. The CCC between two signals is shown in Figure 3.1c. A sharp peak in CCC has 1 second shift from the origin.

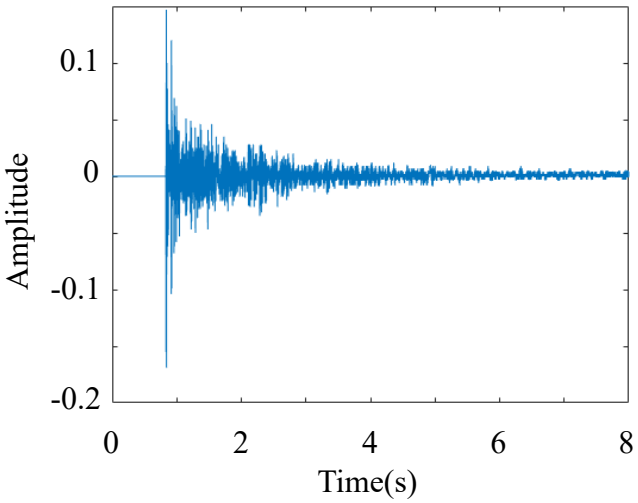

(a)

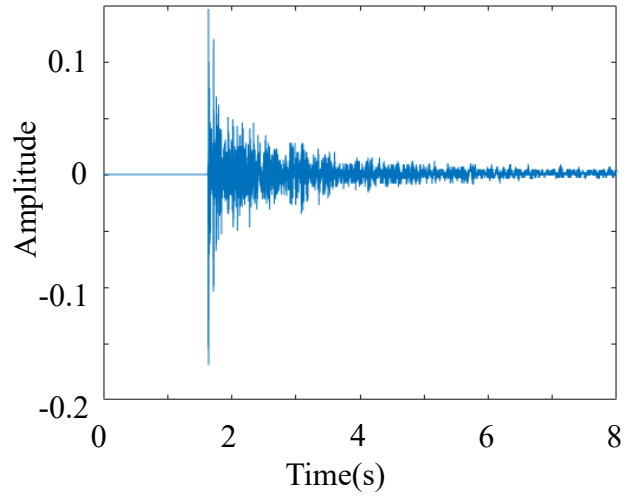

(b)

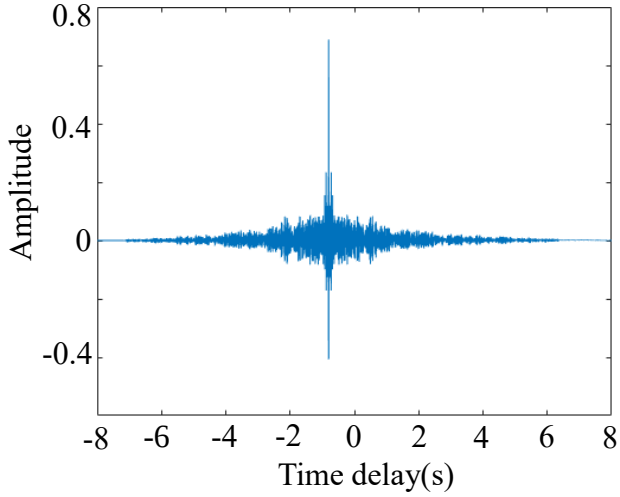

(c)

Figure 3.1 An example to estimate the time delay between two signals using CCC (a) An impulse response signal, (b) The same signal delayed by 1 second, (c) Cross-correlation coefficient.

3.2.2 Cross-correlating continuous signals in the frequency domain

The CCF can also be computed in the frequency domain. The Fourier transforms $X_1(f)$ and $X_2(f)$ of signals $x_1(t)$ and $x_2(t)$ are given by

$$X_b(f) = \int_{-\infty}^{\infty} x_b(t) e^{-j2\pi ft} dt, \qquad (3.6)$$

where $b=1,2$ and the inverse Fourier transform (IFT) is given by

$$x_b(t) = \int_{-\infty}^{\infty} X_b(f) e^{j2\pi ft} df. \quad (3.7)$$

Substituting the value of $X_2(t)$ with $b=2$ from Equation 3.6 into Equation 3.4, produces

$$\hat{R}_{x_1x_2}(\tau) = \frac{1}{T} \int_0^{T-\tau} x_1(t) \int_{-\infty}^{\infty} X_2(f) e^{j2\pi f(t+\tau)} df dt. \quad (3.8)$$

This can be rearranged to give

$$\hat{R}_{x_1x_2}(\tau) = \frac{1}{T} \int_{-\infty}^{\infty} X_2(f) \int_0^{T-\tau} x_1(t) e^{-j2\pi(-f)t} e^{j2\pi f\tau} dt df \quad (3.9)$$

Or

$$\hat{R}_{x_1x_2}(\tau) = \frac{1}{T} \int_{-\infty}^{\infty} X_2(f) X_1(-f) e^{j2\pi f\tau} df. \quad (3.10)$$

Since

$$X_1(-f) = |X_1(f)| e^{-j2\pi ft} = X_1^*(f), \quad (3.11)$$

Equation 3.10 can be rearranged to give

$$\hat{R}_{x_1x_2}(\tau) = \frac{1}{T} \int_{-\infty}^{\infty} X_1^*(f) X_2(f) e^{j2\pi f\tau} df, \quad (3.12)$$

where * denotes the complex conjugate. From Equation 3.12, the CCF between two signals $x_1(t)$ and $x_2(t)$ in the frequency domain is the IFT of the product of complex conjugate of Fourier transform of signal $x_1(t)$ and Fourier transform of signal $x_2(t)$ [74], which is depicted in Figure 3.2.

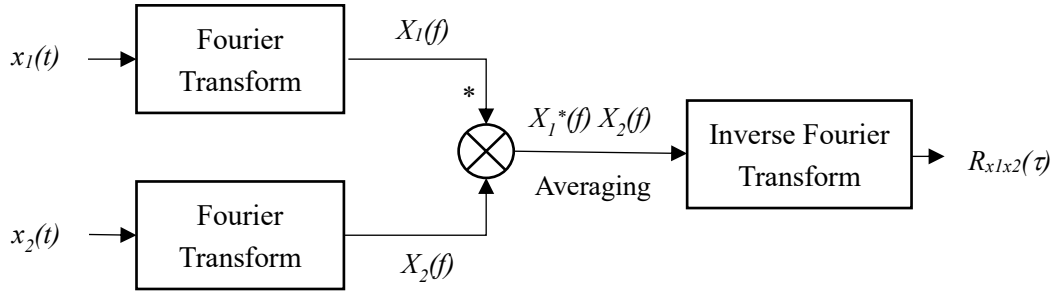

Figure 3.2 Schematic diagram of implementing CCF in the frequency domain.

Involving fewer calculations is the advantage of performing the CCF in the frequency domain [75]. The disadvantage is that for a fixed sampling frequency f_s, the maximum time delay τ_{max} which can be measured depends upon the length N of the Fourier Transform, i.e., $\tau_{max} \propto N/f_s$. The Fourier Transform is usually calculated by using Fast Fourier Transform (FFT) for discrete signals. If the CCF is calculated by using a longer sequence signal, its calculation amount will increase dramatically.

3.2.3 CCF for discrete leak-induced signals

In this study, the CCF is performed directly on these discrete digital signals measured by AE sensors. If the two leak-induced signals are $x_1(n)$ and $x_2(n)$ for $m>0$, $n= 0, 1, ..., N - 1$, then the biased CCF is given by

$$\hat{R}_{x_1x_2}(m) = \frac{1}{N}\sum_{n=0}^{N-1-m} x_1(n)x_2(n+m),$$
$$\hat{R}_{x_1x_2}(-m) = \frac{1}{N}\sum_{n=0}^{N-1-m} x_2(n)x_1(n+m). \qquad (3.13)$$

Equation 3.13 is tedious to compute due to lots of time shifting (n+m). However, the signal process can be easier by performing CCF in the frequency domain using FFT. In this case, $x_1(t)$ and $x_2(t)$ are replaced with $x_1(n)$ and $x_2(n)$ and the FFTs are denoted by $X_1(f)$ and $X_2(f)$ respectively. The cross-correlation function $R_{x1x2}(\tau)$ is computed by taking the inverse FFT of $X_1^*(f)X_2(f)$ and scaled appropriately, where $X_1^*(f)$ denotes the complex conjugation of the FFT of $x_1(n)$ and $X_2(n)$ is the FFT of $x_2(n)$. This method also has the same problem that its calculation amount increases if the FFT length (N) increases.

3.3 GCC method for leakage location

The schematic diagram of the implementation of GCC function is shown in Figure 3.3, a weighting estimator is applied to the cross-spectral density (CSD) function before performing the IFT [76]. The weighting estimator has two effects:

(1) Enhance signals in the frequency bands with a high signal-to-noise ratio (SNR) and suppressing signals outside these bands [77].

(2) Sharpen the peak in the CCF [78].

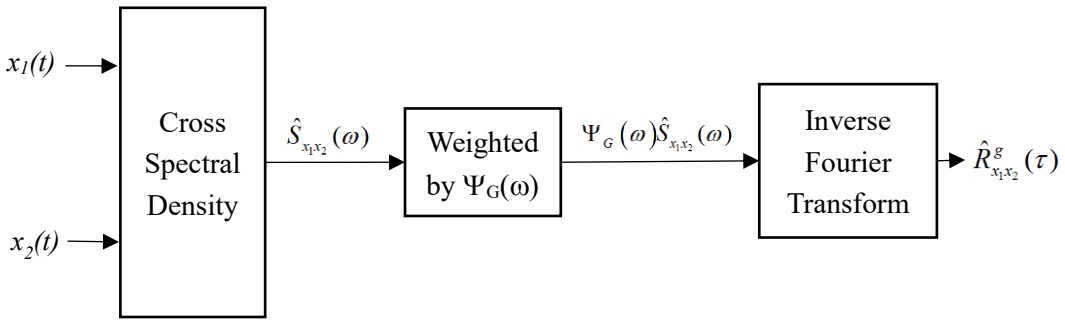

Figure 3.3 Schematic diagram of the implementation of GCC function in the frequency domain.

There are several types of GCC weighting estimators:

(1) Phase transform (PHAT)

(2) Smoothed coherence transforms (SCOT)

(3) Maximum likelihood (ML) estimator

The biased GCC estimator $R_{x1x2}{}^g(\tau)$ for the finite time duration (T) signals $x_1(t)$ and $x_2(t)$ is given by

$$\hat{R}^g_{x_1x_2}(\tau) = F^{-1}\left\{\Psi_G(\omega)\hat{S}_{x_1x_2}(\omega)\right\} = \frac{1}{2\pi}\int_{-\infty}^{+\infty}\Psi_G(\omega)\hat{S}_{x_1x_2}(\omega)e^{j\omega\tau}d\omega, \qquad (3.14)$$

where $F^{-1}\{\}$ denotes the IFT, $\Psi_g(\omega)$ is the GCC weighting estimator and $\hat{S}_{x_1x_2}(\omega)$ represents the estimate of CSD, which is given by

$$\hat{S}_{x_1x_2}(\omega) = \frac{1}{2\pi n_a T} \sum_{b=1}^{n_a} X_{1_b}^*(\omega, T) X_{2_b}(\omega, T), \qquad (3.15)$$

where n_a stands for the total number of averages over the duration T. The three weighting functions (SCOT, ML and PHAT) are mentioned in Table 3.1. Since all the weighting functions are real numbers, they have no effect on the phase of CSD. $\Psi_g(\omega)$ should be chosen when a sharp peak in CCF is obtained. However, sharp peaks are more sensitive to errors introduced by finite observation time, particularly in cases of low SNR. Thus, the choice of $\Psi_g(\omega)$ is a compromise between good resolution and stability[79].

Table 3.1 Various GCC weighting estimators.

estimator	PHAT	SCOT	ML
$\Psi_G(\omega)$	$\frac{1}{\lvert S_{x_1x_2}(\omega)\rvert}$	$\frac{1}{\sqrt{S_{x_1x_1}(\omega)S_{x_2x_2}(\omega)}}$	$\frac{\gamma^2_{x_1x_2}(\omega)}{\left[1-\gamma^2_{x_1x_2}(\omega)\right]}\frac{1}{\lvert S_{x_1x_2}(\omega)\rvert}$

where $\gamma_{x_1x_2}(\omega) = \frac{S_{x_1x_2}(\omega)}{\sqrt{S_{x_1x_1}(\omega)S_{x_2x_2}(\omega)}}$.

3.3.1 PHAT estimator

The frequency weighting function of the PHAT estimator[80] is given by

$$\Psi_P(\omega) = \frac{1}{\lvert S_{x_1x_2}(\omega)\rvert}, \qquad (3.16)$$

where subscript P stands for PHAT estimator. Substituting in Equation 3.14 will give

$$\hat{R}^{P}_{x_1x_2}(\tau) = F^{-1}\left\{\Psi_P(\omega)\hat{S}_{x_1x_2}(\omega)\right\} = \frac{1}{2\pi}\int_{-\infty}^{+\infty}\frac{\hat{S}_{x_1x_2}(\omega)}{\left|S_{x_1x_2}(\omega)\right|}e^{j\omega\tau}d\omega = \delta(\tau+T), \quad (3.17)$$

where $\delta(\tau+T)$ represents the Dirac delta function delayed by time $-T$. The PHAT estimator makes the output of the CCF become a delta function [81], which is a narrow peak. However, it will happen only when $\hat{S}_{x_1x_2}(\omega) = \left|S_{x1x2}(\omega)\right|$, and this method takes no account of noise in the signals $x_1(t)$ and $x_2(t)$, which enlarges location errors, especially when the SNR is low.

3.3.2 SCOT estimator

The frequency weighting function of the SCOT estimator is written as

$$\Psi_S(\omega) = \frac{1}{\sqrt{S_{x_1x_1}(\omega)S_{x_2x_2}(\omega)}}. \quad (3.18)$$

Substituting in Equation 3.14 to have

$$\hat{R}^{S}_{x_1x_2}(\omega) = F^{-1}\left\{\Psi_S(\omega)\hat{S}_{x_1x_2}(\omega)\right\} = \frac{1}{2\pi}\int_{-\infty}^{+\infty}\frac{\hat{S}_{x_1x_2}(\omega)}{\sqrt{S_{x_1x_1}(\omega)S_{x_2x_2}(\omega)}}e^{j\omega\tau}d\omega \quad (3.19)$$

Or

$$\hat{R}^{S}_{x_1x_2}(\omega) = \frac{1}{2\pi}\int_{-\infty}^{+\infty}\hat{\gamma}_{x_1x_2}(\omega)e^{j\omega\tau}d\omega = h_s(\tau)\otimes\delta(\tau+T), \quad (3.20)$$

where $\hat{\gamma}_{x_1x_2}(\omega) = \dfrac{\hat{S}_{x_1x_2}(\omega)}{\sqrt{S_{x_1x_1}(\omega)S_{x_2x_2}(\omega)}}$ is the coherence estimate of signals $x_1(t)$ and $x_2(t)$, and $h_s(\tau) = F^{-1}\left\{\dfrac{\hat{S}_{x_1x_2}(\omega)}{\sqrt{S_{x_1x_1}(\omega)S_{x_2x_2}(\omega)}}\right\}$. Substituting $\hat{\gamma}_{x_1x_2}(\omega)$ in Equation 3.18 to have

$$\Psi_S(\omega) = \frac{\hat{\gamma}_{x_1x_2}(\omega)}{\left|\hat{S}_{x_1x_2}(\omega)\right|}. \quad (3.21)$$

The SCOT estimator can be interpreted as two filtering processes: signal whitening can be done by the denominator; the numerator can sharpen the peak in the CCF.

Therefore, the SCOT estimator can both sharpen the peak and whiten the leak-induced signal.

3.3.3 ML estimator

The frequency weighting function of the ML estimator is given by

$$\Psi_M(\omega) = \frac{\hat{\gamma}^2_{x_1x_2}(\omega)}{1-\hat{\gamma}^2_{x_1x_2}(\omega)} \frac{1}{\left|\hat{S}_{x_1x_2}(\omega)\right|}. \qquad (3.22)$$

Substituting in Equation 3.14 to have

$$\hat{R}^M_{x_1x_2}(\tau) = F^{-1}\left\{\Psi_M(\omega)\hat{S}_{x_1x_2}(\omega)\right\} = h_M(\tau) \otimes \delta(\tau + T_0), \qquad (3.23)$$

where $h_M(\tau) = F^{-1}\left\{\frac{\hat{\gamma}^2_{x_1x_2}(\omega)}{1-\hat{\gamma}^2_{x_1x_2}(\omega)} \frac{\hat{S}_{x_1x_2}(\omega)}{\left|\hat{S}_{x_1x_2}(\omega)\right|}\right\}$, there are two pre-filtering operations involved in the ML estimator. The first term $\frac{\hat{\gamma}^2_{x_1x_2}(\omega)}{1-\hat{\gamma}^2_{x_1x_2}(\omega)}$ sharpens the peak in the CCF; the second term $\frac{1}{\left|\hat{S}_{x_1x_2}(\omega)\right|}$ can whiten the leak-induced signal. However, $\Psi_M(\omega)$ will approach infinity if $\gamma^2_{x_1x_2}(\omega)$ is close to one. Therefore, this estimator is not preferable to the SCOT estimator for leak detection as it has the effect of overemphasizing as well as underemphasizing signals at certain frequencies.

3.4 The parameters affecting the CCF of leak-induced signals

The location accuracy of the cross-correlation method for leak detection depends upon three parameters:

(1) The distance between two sensors,

(2) Estimation of the time delay between two measured signals,

(3) The propagation velocity of leak-induced signals in the pipe.

The distance between sensors can be measured for the straight pipe lengths. The unexpected loops or bends can cause an error in accuracy with the pipe length. The following research work is divided into two parameters: the estimation of time delay and the propagation velocity of leak-induced signals in pipes.

The time delay between two measured signals is estimated by the CCF. The parameters affecting CCF peak are listed in Table 3.2 and are discussed below.

Table 3.2 Parameters affecting CCF of leak-induced signals.

Magnitude	Frequency domain	Noise (*dB*)	Attenuation (*dB/m*)	Weighting factor	Observation time
$x_1(t)$, $x_2(t)$	$X_1(f)$, $X_2(f)$	n_1, n_2	α	$\Psi_G(\omega)$	T

(1) Measured leak-induced signals $x_1(t)$ and $x_2(t)$: the sharpness and the magnitude of CCF peak are affected by the four main characteristics of two measured signals:

a) Magnitude: It can be interpreted from Equation 3.1 that the measured signals $x_1(t)$ and $x_2(t)$ are the combination of leak-induced signals $s_1(t)$, $s_2(t)$ and noise n_1 and n_2.

b) Signal acquisition duration: The signals measured by each sensor travels different distances from the leak source. Consequently, the duration over which signals are measured should be long enough so that the measured signals contain enough time domain information to obtain a sharp CCF peak [82].

c) Frequency response: Frequency response of pipes determines the frequency

range of leak-induced signals, which helps in selecting cut-off frequencies, data acquisition card and sensors [83]. Improper selection of frequency range will cause an error or even no peak at all.

d) Phase: The phase of leak-induced signals is important to determine the time delay between two measured signals.

(2) Fourier Transform: The Fourier transform is commonly computed by FFT, and the maximum time delay which can be measured depends upon the length of FFT. It is essential to optimize the length of FFT to decrease the calculations amount and increase the time delay measurement range.

(3) Noise intensity: The measured signals are a combination of leak-induced signals and the noise. If the noise intensity dominates the measured signals, the noise may fade the actual leak-induced signals and increase the location error.

(4) Signals attenuation: Signals attenuation with the propagation distance of leak-induced signals along the pipe depends upon the pipe material. It limits the maximum measurable distance between sensors and the leak source.

(5) Weighting factor: a weighting factor sharpens the cross-correlation peak and eliminates the frequencies components with low SNR. The cross-correlation peak is sensitive to the background noise, therefore, the choice of weighting factor should be the compromise between high accuracy and stability.

(6) Measurement duration: CCF is significantly affected by the SNR. If the signal length used to calculate the delay is too long, the amount of computation will increase, otherwise, the time delay between two measured signals will be missed.

The variables discussed above significantly affect the location accuracy, so their optimization is necessary to obtain accurate time delay estimation.

The second parameter affecting the location accuracy is the propagation velocity of leak-induced signals in pipes, which can be calculated by a theoretical formula and the pipe physical properties or by measuring on-site. Since the wave velocity varies with pipe physical characteristics and leak-induced signal characteristics, it is difficult to calculate its exact value.

In addition to the parameters discussed above, there are several other parameters which either indirectly or directly affect the location accuracy discussed below:

(1) Sensitivity of sensors: This determines the ability of sensors to measure weak signals. A highly sensitive sensor picks up more background noise, while a low sensitivity sensor will miss the weak signals. The peak frequency of the leak-induced signal is proportional to the gas jet velocity and inversely proportional to the leakage aperture [10], and it's also related to the resonant frequency of the sensor and the distance between the leak and the sensor. Therefore, an optimum choice of sensors is required for measuring different leak-induced signals.

(2) Gas pressure: For a fixed dimensional leak orifice, an increase in gas pressure enhances the magnitude of leak-induced signals [84].

(3) The sharpness of cross-correlation peak: It is preferable to have a sharp cross-correlation peak. However, it is difficult to obtain a sharp cross-correlation peak in practice due to signal dispersion, background noise and finite measurement duration.

(4) The similarity of leak-induced signals: The higher the similarity between two

measured signals, the higher the location accuracy.

(5) Filters: Signals obtained from the sensors needs to be filtered to remove background noise. However, due to poor knowledge about the characteristics of leak-induced signals, it is difficult to select appropriate cut-off filter frequencies for the filter.

3.5 Conclusions

The cross-correlation method for leak detection is based on the characteristics of leak-induced signals in pipes. Due to limited knowledge of the characteristics of leak-induced signals in pipes, this method is difficult to employ in pipes. Some parameters such as filter cut-off frequencies, weighting factor, observation time, etc. and hardware components, such as sensors and signal acquisition card, etc. require optimization when a leak between two sensors is located.

In this chapter, the calculation of the CCF in the time domain and frequency domain is presented. It is concluded that the frequency domain analysis eliminates the need for selection of cut-off frequencies, but at the expense of a small loss of accuracy. It is also concluded that the maximum value of time delay which can be measured is limited by the length of FFT. Various time-delay estimators used in GCC are also compared for leak detection in pipes. It has been shown that the PHAT, SCOT and ML estimators designed to pre-filter the leak-induced signals prior to the CCF can sharpen the peak in the CCF. The PHAT estimator is designed to give a delta function, the SCOT and ML estimators additionally take account of the effect of background noise in the estimation procedure. ML estimator has the effect of overemphasizing or underemphasizing at certain frequencies.

Chapter 4 Wave velocity measurement theory

In practice, the pipes have many discontinuities in dimensions, which makes it difficult to determine the propagation speed by using existing theoretical and experimental approaches. In this chapter, the method for calculating the speed of leak-induced signals in a gas pipe is proposed and experimentally verified.

Wave velocity depends upon the dimensions and material properties of the pipe wall, and it can be determined by using various theoretical and experimental methods mentioned below:

(1) Analytical method,

(2) Time-of-flight method,

(3) Cross-correlation method,

(4) Three sensor method,

(5) Phase-frequency method for calculation of speed,

(6) Modal analysis of guided waves.

4.1 Analytical method

This method is based on the theoretical relationship between the physical properties of pipe and the speed of leak-induced signals [85], therefore, the size and physical properties of the pipe needs to be determined before calculating the wave velocity. The wavenumber for the waves at frequencies below the ring frequency of the pipe can be

written as

$$k^2 = k_f^2(1+\frac{2B_f a}{Eh+j\eta Eh}), \qquad (4.1)$$

where η is the pipe loss factor, E is elastic modulus, h is the thickness of the pipe, B_f is fluid bulk modulus, k_f is the fluid wavenumber, rearranging Equation 4.1 to have

$$k^2 = k_f^2\left[1+\frac{2B_f a}{Eh(1-\eta^2)} - j\frac{2B_f a\eta}{Eh(1-\eta^2)}\right]. \qquad (4.2)$$

The pipe loss factor η is much less than unity, thus the term η^2 can be neglected as

$$k^2 = k_f^2\left[1+\frac{2B_f a}{Eh} - j\frac{2B_f a\eta}{Eh}\right] = Q + jS, \qquad (4.3)$$

where $Q = k_f^2(1+\frac{2B_f a}{Eh})$ and $S = k_f^2(-\frac{2B_f a\eta}{Eh})$. The wavenumber k is complex and assuming that $k = k_R + jk_I$, then Equation 4.3 becomes

$$Q + jS = (k_R + jk_I)^2 = k_R^2 - k_I^2 + 2jk_R k_I, \qquad (4.4)$$

where k_R and k_I represent the real and imaginary components of the wavenumber k. Comparing the real and imaginary components in Equation 4.3, and rearranging to have

$$4k_R^4 - 4k_R^2 Q - S^2 = 0. \qquad (4.5)$$

The solution of the above equation is given by

$$k_R^2 = \frac{Q \pm \sqrt{Q^2+S^2}}{2}. \qquad (4.6)$$

As k_R and k_I are real numbers, considering only positive terms in Equation 4.6, will give:

$$k_R = \sqrt{\frac{Q+\sqrt{Q^2+S^2}}{2}} \quad \text{and} \quad k_I = \frac{S}{\sqrt{2(Q+\sqrt{Q^2+S^2})}}. \qquad (4.7)$$

Substituting the value of Q and S, and neglecting the higher order terms of η to give

$$k_R = k_f \sqrt{1 + \frac{2B_f a}{Eh}} \qquad (4.8)$$

and

$$k_I = \frac{k_f \left(-\frac{2B_f a\eta}{Eh}\right)}{2\sqrt{1 + \frac{2B_f a}{Eh}}}. \qquad (4.9)$$

The wavenumber k is related to the speed c and attenuation α of leak-induced signals by

$$k = \frac{\omega}{c} - j\alpha\omega, \qquad (4.10)$$

Equating the real and imaginary parts in Equation 4.8, 4.9 and 4.10 to give the wave speed as

$$c = \omega / \mathrm{Re}(k) = \omega / \left(k_f \sqrt{1 + \frac{2B_f a}{Eh}}\right) = c_f \left(1 + \frac{2B_f a}{Eh}\right)^{-1/2}, \qquad (4.11)$$

and the attenuation is given by

$$\alpha = -\frac{\mathrm{Im}\{k\}}{\omega} = \frac{k_f \left(\frac{B_f a\eta}{Eh}\right)}{\omega\sqrt{1 + \frac{2B_f a}{Eh}}} = \frac{1}{c_f} \frac{\frac{B_f a\eta}{Eh}}{\sqrt{1 + \frac{2B_f a}{Eh}}}, \qquad (4.12)$$

where c_f is the fluid speed. It can be inferred from Equation 4.11 that the wave speed is independent of frequency but is dependent on the dimensions and Young's modulus of pipe. In Equation 4.12, the attenuation of leak-induced signals depends upon the stiffness of pipe material. Metallic pipes have more stiffness than plastic pipes, therefore, they have lower attenuation than plastic ones.

4.2 Time-of-flight method

Time-of-flight is a common method to determine the speed of leak-induced signals in pipes[86]. In this method, propagation speed is calculated based on the time delay between the transient signals. Wave velocity is equal to the quotient of propagation distance and the time delay. The transient signals can be generated when the pipe was tapped by the impact hammer. In the out-of-bracket source method, the source of transient signals lies outside of the two sensors; in the in-bracket source method, the source of transient signals lies between two sensors. For example, the signals were measured by two sensors, the distance between the vibration source and two sensors are 5.7m and 6.8m respectively, and the distance between two sensors is 12.5mm. The times of flight calculated for two sensors were 0.00237 seconds and 0.00285 seconds respectively and the corresponding velocities were 2402m/s and 2384m/s.

4.3 Cross-correlation method

The cross-correlation method is similar to the time-of-flight method. In the cross-correlation method, the wave velocity is estimated based on the time delay between two continuous signals measured by two sensors and the distances between two sensors. The velocity is calculated by dividing the distance difference away from the vibration source to two sensors by the time delay between two measured signals. The velocity of leak-induced signals can be calculated using Equation 3.2. The accuracy of the cross-correlation method for calculating velocity depends upon the sharpness of the cross-correlation peak. The cross-correlation method is based on the similarity between two

measured signals [87], which is affected by dispersion and frequency-dependent attenuation along the pipe. Therefore, the closer the distances between the simulated leak orifice and two sensors, the more similar two measured signals are.

4.4 Three sensor method

The three-sensor method measures the speed and attenuation of leak-induced signals in pipes using the transfer function between signals measured by three sensors mounted at three locations. To determine the transfer function, the length of a pipe is assumed to be l, and the energy of the leak-induced signals measured at the leak position is assumed to be p_0. Three sensors should have similar characteristics for higher leakage location accuracy. The distance between sensors is the same in Figure 4.1, i.e. $\triangle x_1 = \triangle x_2 = \triangle x$. Assuming the reference point for the transfer function as the point x_2, the acoustic pressures $p_1(\omega, x_1)$, $p_2(\omega, x_2)$ and $p_3(\omega, x_3)$ at positions x_1, x_2 and x_3 along the pipe are given by

$$\begin{aligned} p_1(\omega, x_1) &= P_0(\omega)e^{j(\omega t - kx_1)}, \\ p_2(\omega, x_2) &= P_0(\omega)e^{j(\omega t - kx_2)}, \\ p_3(\omega, x_3) &= P_0(\omega)e^{j(\omega t - kx_3)}. \end{aligned} \qquad (4.13)$$

Therefore,

$$\begin{aligned} &\frac{1}{2}(H_{12} + H_{32}) = \frac{p_1(\omega, x_1) + p_3(\omega, x_3)}{2p_2(\omega, x_2)} = \frac{P_0(\omega)e^{j(\omega t - kx_1)} + P_0(\omega)e^{j(\omega t - kx_3)}}{2P_0(\omega)e^{j(\omega t - kx_2)}} \\ &= \frac{1}{2}\left[e^{-jk(x_1 - x_2)} + e^{-jk(x_3 - x_2)}\right] = \frac{1}{2}\left[e^{jk\Delta x} + e^{-jk\Delta x}\right] = \cos k\Delta x, \end{aligned} \qquad (4.14)$$

where H_{12} is the transfer function between sensor 1 and 2, which is defined as $p_1(\omega, x_1)/ p_2(\omega, x_2)$, and H_{32} is the transfer function between sensor positions 3 and 2 defined as $p_3(\omega, x_3)/ p_2(\omega, x_2)$.

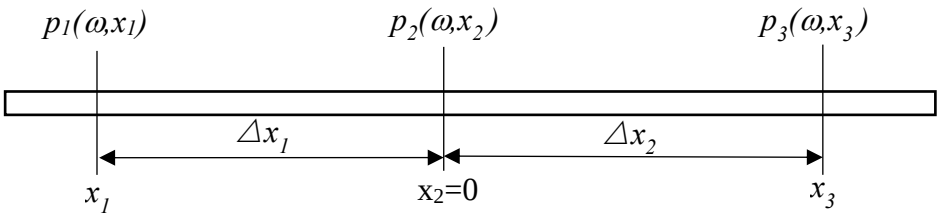

Figure 4.1 Schematic of pressure transducers along the pipe.

Thus, the wavenumber k is related to the three pressures as

$$k = \frac{1}{\Delta x}\arccos\left(\frac{H_{12}+H_{32}}{2}\right) = \frac{1}{\Delta x}\arccos\left(\frac{p_1(\omega,x_1)+p_3(\omega,x_3)}{2p_2(\omega,x_2)}\right). \quad (4.15)$$

Substituting the value of $k = \omega/c - j\alpha\omega$, the transfer function can be expressed as

$$H(\omega,\Delta x) = e^{-j\omega\Delta x/c}e^{-\alpha\Delta x}. \quad (4.16)$$

With this expression for the transfer function, Equation 4.15 can be rewritten as

$$\frac{1}{2}(H_{12}+H_{32}) = \cos(\omega\Delta x/c)\cosh(\alpha\Delta x) + j\sin(\omega\Delta x/c)\sinh(\alpha\Delta x). \quad (4.17)$$

The transfer functions H_{12} and H_{32} are calculated from the three pressure measurements. The wavenumber and speed are calculated from the real part of measured transfer functions, while the attenuation coefficient is calculated from the imaginary part of measured transfer functions using Equation 4.15 and 4.17.

4.5 Phase-frequency method for leakage location

Among all the methods discussed above, CCF is the basic method to measure the velocity of leak-induced signals.

The method based on the phase-frequency relationship of leak-induced signals is proposed in this section. It was found that both the individual and relative phase of leak-

induced signals vary linearly with frequency and the time delay can be calculated from the slope of the linear phase-frequency relationship. The schematic of estimating time delay by using a linear phase-frequency relationship method is shown in Figure 4.2. To calculate the speed of leak-induced signals, the Fourier Transform of two leak-induced signals are multiplied and averaged over a theoretically infinite observation interval (T) to have

$$S^m_{x_1x_2}(\omega) = \underset{T\to\infty}{Lim}\frac{1}{T}\int_{-\infty}^{\infty}\int_{-\infty}^{\infty}(P_0(\omega))^2 e^{-\omega\alpha(l_1+l_2)}e^{-j\omega(l_1+l_2)/c}dfd\tau = S_{ll}(\omega)\Psi(\omega)e^{-j\omega(l_1+l_2)/c}, \quad (4.18)$$

where l_1 and l_2 are the respective distances between sensor 1 and 2 and leak source, $S_{ll}(w)$ is the ASD of leak-induced signals and

$$\Psi(\omega) = e^{-\omega\alpha(l_1+l_2)} = e^{-\omega\alpha l}, \quad (4.19)$$

where l is the distance between two sensors. The argument of Equation 4.18 gives the phase as

$$\varphi^m_{x_1x_2}(\omega) = Arg\left\{S^m_{x_1x_2}(\omega)\right\} = -\omega(l_1+l_2)/c = -l\omega/c, \quad (4.20)$$

It can be inferred that the phase of the product of Fourier Transform of leak-induced signals measured by two sensors mounted at two locations varies linearly with frequency w. The velocity can be calculated from the slope of the linear relationship between $\varphi^m_{x_1x_2}(\omega)$ and frequency. This method requires the total distance l between the two sensors. The main important index of this method is the coherence between signals. The higher the coherence, the better the results will be, so the signal measurements on shorter sensor spacings are preferred.

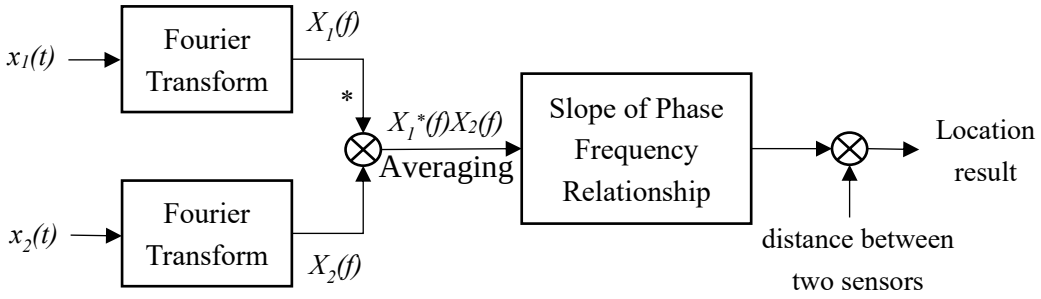

Figure 4.2 Schematic diagram of leakage location method using the phase-frequency relationship of leak-induced signals.

4.6 Modal analysis of guided waves

Since the gas-solid coupling between the in-pipe gas and the pipe wall can be ignored due to the acoustic impedance mismatch between them, the gas-filled pipes can be approximated as hollow cylinders [9]. The dispersive behaviors of the guided waves in a gas pipe can be analyzed by the guided wave theory of the hollow cylinders [88]. The guided waves in a pipe are grouped into three families: longitudinal mode, torsional mode, and flexural mode. These modes are denoted by *L(0,m)*, *T(0,m)* and *F(n,m)*, respectively, where *n* and *m* represent the circumferential and radial modal parameters[89], respectively. The theoretical analysis shows that the radial vibration signal collected by AE sensors is dominated by the dispersive fundamental flexural mode *F(1,1)* [90].

The material and geometric parameters of the given pipe are shown in Table 5.1. According to the parameters of the given pipe, the group speed dispersive curves of the flexural modes shown in Figure 4.3 can be obtained using the guided wave theory of hollow cylinders in MATLAB R2018b [91]. The speed of the AE signal can be online estimated by the peak frequency of the AE signal in combination with the known group speed dispersive curve of the fundamental flexural mode [9].

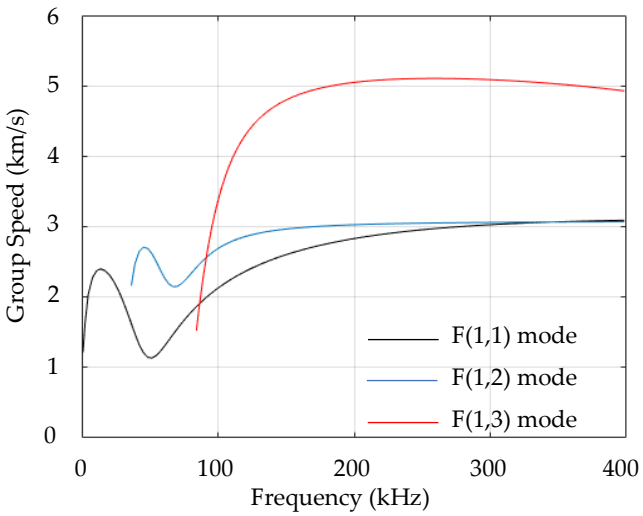

Figure 4.3 Group speed dispersive curves of the flexural modes in the frequency band 0–400 kHz for the given gas pipe.

Table 4.1 Material and geometric parameters of the given pipe.

a(mm)	*b(mm)*	μ	$\rho(kg/m^3)$	*G(GPa)*	*E(GPa)*
13.9	16.7	0.35	8000	76	205

a is the inner radius of the pipe,
b is the outer radius of the pipe,
μ is the Poisson's ratio of the pipe wall material,
ρ is the density of the pipe wall material,
G is the shear modulus of the pipe wall material,
E is Young's modulus of the pipe wall material.

4.7 Conclusions

Velocity and attenuation of leak-induced signals with distance play an important role in locating a leak using the cross-correlation method. Wave velocity can be approximated using the analytical method, time-of-flight method, cross-correlation method, three sensors methods and phase-frequency method, which are presented in this chapter. These methods require prior knowledge of the pipe physical properties and a known leak-induced signal/transient event source. and the presence of discontinuities in the pipe will affect the wave velocity. These methods don't consider the dispersion characteristics of the AE signal, therefore, a new method based on the dispersion characteristics of the AE signal is proposed in chapter 4.1.6.

The AE signal group velocity changes with the frequency due to the dispersion characteristics of the AE wave group velocity, so the peak frequency of the AE signal needs to be determined before determining the wave velocity, then the speed of the AE signal can be online estimated by the peak frequency of the AE signal in combination with the known group speed dispersive curve of the fundamental flexural mode. This method for determining the wave velocity can effectively eliminate the effects of noise, so this method will be used to determine the AE signal velocity in this study.

Chapter 5 Filter based on wavelet transform and empirical mode decomposition

5.1 Brief review of the wavelet theory

5.1.1 The wavelet transform

The continuous wavelet transform (CWT) of the signal *s(t)* with the analyzing wavelet $\psi(t)$ is the convolution of *s(t)* with a scaled and conjugated wavelet

$$W(\alpha,b)=\alpha^{-1/2}\int_{-\infty}^{\infty}s(t)\psi^{*}\left(\frac{t-b}{\alpha}\right)dt, \qquad (5.1)$$

The wavelet coefficient $W(\alpha,b)$ measures the similarity between the signal *s(t)* and the analyzing wavelet $\psi(t)$ at different scales as defined by the parameter α, and different time positions as defined by the parameter *b*. The factor $\alpha^{-1/2}$ is used for energy preservation. Equation 5.1 indicates that the wavelet analysis is a time-frequency analysis. The frequency segmentation is obtained by translation and dilation of the analyzing wavelet. At successively larger scales, the frequency resolution improves and the time resolution decreases.

The discrete wavelet transform is performed by choosing fixed values $\alpha=2^m$ and $b=n2^m$, where *m* and *n* are integers. Thus, discrete wavelets $\psi_{m,n}(t)=2^{-m/2}\psi(2^{-m}t-n)$ can be constructed, which can also constitute an orthonormal basis. The discrete wavelet analysis can be implemented by the scaling filter *h(n)*, which is a low-pass filter related to the scaling function $\varphi(t)$, and the wavelet filter *g(n)*, which is a high-pass filter

related to the wavelet function $\psi(t)$.

$$h(n) = \frac{1}{\sqrt{2}} \langle \varphi(t), \varphi(2t-n) \rangle, \tag{5.2}$$

$$g(n) = \frac{1}{\sqrt{2}} \langle \phi(t), \phi(2t-n) \rangle = (-1)^n h(1-n) \tag{5.3}$$

The properties of the filters have been widely analyzed [92]. A fast wavelet algorithm is illustrated in Figure 5.1 and can be implemented by decomposition and reconstruction.

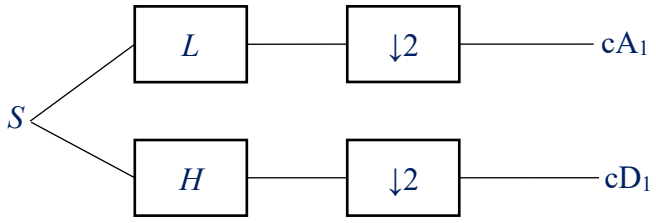

(a) Decomposition

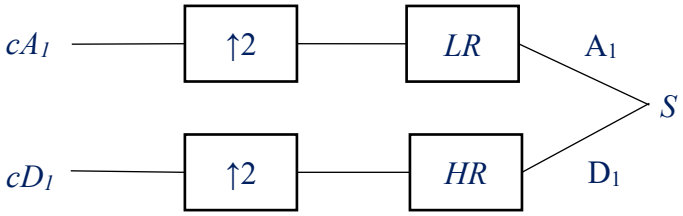

(b) Reconstruction

Figure 5.1 Basic step of decomposition and reconstruction of the wavelet transform

In the decomposition step in Figure 5.1(a), the discrete signals s is convolved with a low pass filter L and a high pass filter H, resulting in two vectors cA_1 and cD_1.

The elements of the vector cA_1 are called Approximation Coefficients and the elements of the vector cD_1 are called Detail Coefficients. The symbol ↓2 denotes downsampling, i.e. omitting the odd indexed elements of the filtered signal, so that the number of the coefficients is approximately the same as the number of elements of the

discrete signal *s*.

In the reconstruction step in Figure 5.1(b), a pair of low-pass and high-pass reconstruction filters *LR* and *HR* are convolved with the vectors cA_1 and cD_1, respectively. Two signals are produced resulting in a reconstruction signal A_1 called Approximation, and a reconstruction signal D_1 called Detail. The symbol ↑2 denotes upsampling, e.g. inserting zeros between the elements of the vectors cA_1 and cD_1. An important property of this step is

$$s = A_1 + D_1 \tag{5.4}$$

The procedure of the basic step can be repeated on the approximation vector cA_1 and successively on every new approximation vector cA_j. This concept is presented by means of a wavelet tree with *J* levels, where *J* is the number of iterations of the basic step. In Figure 5.2, the wavelet tree of wavelet decomposition for *J*=3 is illustrated. Each vector *Aj* includes approximately, $N_t/2^j$ coefficients, where N_t is the length of the signal *s*, and provides information about a frequency band $[0, F_s/2^{j+1}]$, where F_s is the sampling rate. The reconstruction signals A_j and D_j satisfy the equations

$$A_{j-1} = A_j + D_j \tag{5.5}$$

$$s = A_j + \sum_{i \le j} D_i \tag{5.6}$$

where *i* and *j* are positive integers.

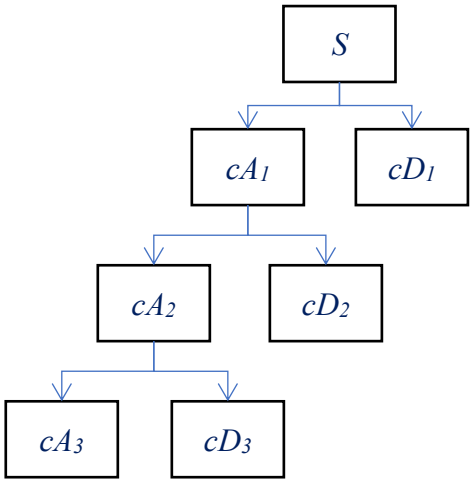

Figure 5.2 An example of a three-level wavelet tree.

5.1.2 The wavelet packet transform

The WPT is a generalization of the wavelet transform. By defining two functions

$$W_0(t) = \varphi(t) \tag{5.7}$$

$$W_1(t) = \psi(t) \tag{5.8}$$

where $\varphi(t)$ and $\psi(t)$ are the scaling and wavelet functions, respectively. In an orthogonal case, the functions $W_n(t)$, $m=0,1,2,..$, can be obtained as

$$W_{2m}(t) = 2\sum_{n=0}^{2N-1} h(n) W_m(2t-n) \tag{5.9}$$

$$W_{2m+1}(t) = 2\sum_{n=0}^{2N-1} g(n) W_m(2t-n) \tag{5.10}$$

$$W_{j,m,n}(t) = 2^{-j/2} W_m\left(2^{-j/2}t - n\right) \tag{5.11}$$

where j is a scale parameter and n is a time localization parameter. The analyzing functions $W_{j,m,n}$ are called wavelet packet atoms.

In practice, a fast algorithm is applied by using the basic step of Figure 5.1. The difference is that both details and approximations are split into finer components,

resulting in a wavelet packet tree. In Figure 5.3, an example of a wavelet packet decomposition tree of three levels is illustrated.

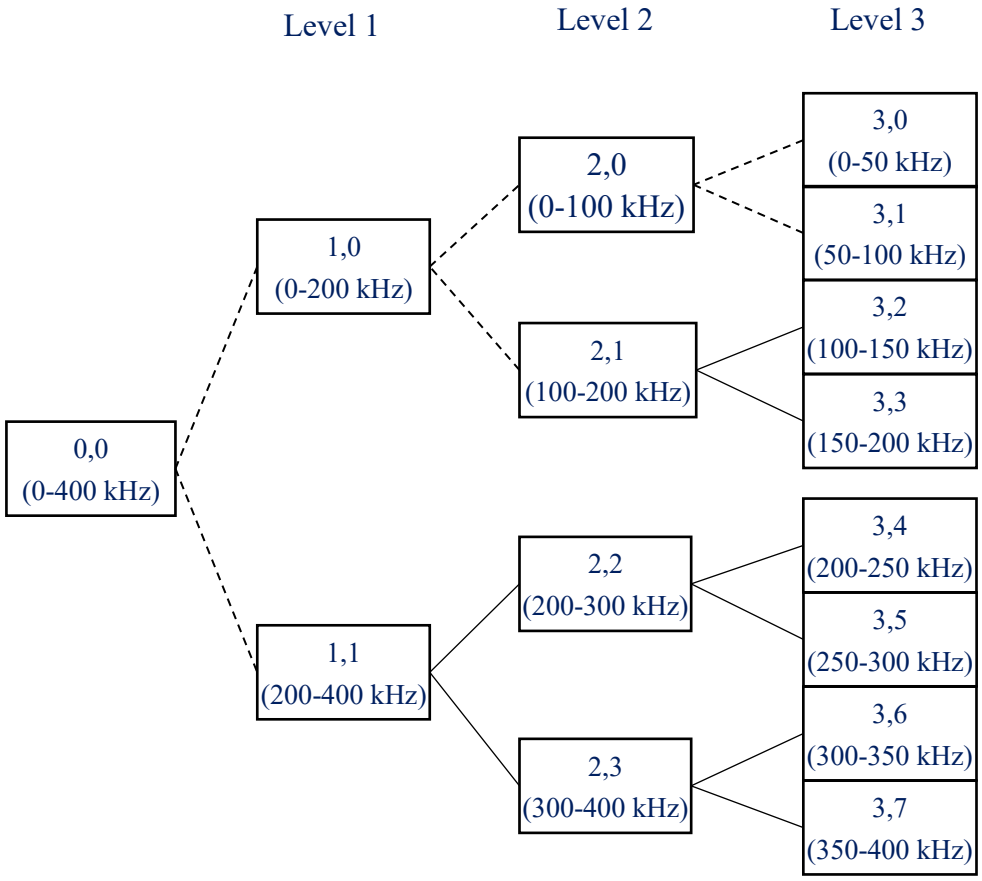

Figure 5.3 An example of a three-level wavelet packet decomposition tree

It is observed that the wavelet tree (dashed line) is a part of the wavelet packet tree. Each node of the wavelet tree is indexed with a integers pair (j, k), where j is the corresponding level of decomposition and k is the order of the node position in the specific level. In each level j, there are 2^j nodes and their order is k=0,1,...,2^j-1. A vector of wavelet packet coefficients $c_{j,k}$ corresponds to each node (j,k), according to the basic step procedure. The length of a vector j,k is approximately $N_t/2^j$. From each vector $c_{j,k}$ a reconstruction signal $R_{j,k}$ of length N_t can be produced, by setting the coefficients of all the other vectors in level j to zero, and by implementing the wavelet packet tree in

the inverse procedure. The width of the frequency range, corresponding to each reconstruction signal $R_{j,k}$ is $F_j \approx Fs/2^{j+1}$. The frequency range corresponding to each node of the wavelet packet tree is shown in Figure 5.3. It is observed that the natural order of the reconstruction signals $R_{j,k}$ in a level j is not the same as the increasing frequency order. This is explained by the fact that low-pass filters may carry information about the high frequency content of the signal, due to frequency folding, caused by downsampling. For example, in the third level of the wavelet tree in Figure 5.3, the natural order is k=0,1,2,..,7, but the frequency order is p=0,1,3,2,7,6,4,5. This fact necessitates the reordering of the wavelet packet vectors $c_{j,p,}$ p=0,1,..,2^j-1, using a new frequency order index p in the level j.

5.2 Brief review of the empirical mode decomposition theory

5.2.1 Empirical mode decomposition

Huang et al.[93] described a new technique for analyzing non-linear and non-stationary data, which is the empirical mode decomposition method. Any complicated data set can be adaptively decomposed into a finite number of intrinsic mode functions. The intrinsic mode function is adopted in that these components represent the oscillation modes contained in the data. In the case of Fourier analysis, oscillation modes in a signal are defined in terms of sine and cosine waves. The EMD defines oscillation modes in terms of IMFs, which are functions that satisfy two conditions:

1. In the whole time-series, the number of extrema and zero crossings should be equal or differ by 1. Note that extrema are either local minima or local maxima. Furthermore, a sample g_i in a time-series is a local maximum if $g_i > g_{i-1}$ and $g_i > g_{i+1}$, and

a sample q_i is a local minimum if $q_i<q_{i-1}$ and $q_i<q_{i+1}$, where i is discrete time.

2. In the time-domain, the mean value of the envelopes is 0, which defined by the local maxima and local minima. This mean is computed for all available samples in the time-domain.

The definition above is empirical and currently there is no explicit equation for estimating IMFs. Thus, any arbitrary time-series that satisfies conditions 1 and 2 is an IMF. Based on the power spectrum of IMFs, it can be verified that these functions represent the original data can be decomposed into different time-domain. This is illustrated by Andrade et al. [94, 95]. Thus, both wavelets and the empirical mode decomposition provide the decomposition of a signal into different time-scales. The main difference is that the former performs the signal decomposition adaptively and based solely on the available data, whereas the latter normally uses a set of pre-fixed filters based on the choice of a mother wavelet.

The EMD method can estimates IMFs. This process is depicted in Figure 5.4. It involves the following steps, leading to a decomposition of the signal *S(t)* into its constituent IMFs:

(1) x (an auxiliary variable) is set to the data *S(t)* to be analyzed, and a variable k is set to zero, which is the number of estimated IMFs.

(2) Splines are fitted to the upper extrema and the lower extrema, which can define the lower (LE) and upper envelopes (UE).

(3) The average envelope, m, is calculated as the arithmetic mean between UE and LE.

(4) A candidate IMF, h, is estimated as the difference between x and m.

(5) If h does not fulfill the criteria defining an IMF, the steps (2)-(4) should be

repeated. Otherwise, if *h* is an IMF then the procedure moves to step 5.

(6) If *h* is an IMF it is saved as c_k, where *k* is the *k*th component.

(7) The mean squared error (MSE) between two consecutive IMFs c_{k-i} and c_k, is calculated, and it is compared to a stopping condition.

(8) If the stopping condition is not reached, the partial residue, r_k, is estimated as the difference between a previous partial residue r_{k-1} and c_k, and its content is assigned to the dummy variable *x* and the steps of (2)-(4) are repeated.

(9) If the stopping condition is satisfied then the process will be finalized and the final residue r_{final} can be estimated based on the difference between *S(t)* and the sum of all IMFs.

The criterion is used to determine whether *h* is an IMF or not, and verify whether *h* satisfies the two conditions.

Currently there is no set of equations to estimate IMFs; therefore, the procedure above is an empirical technique.

When the sifting process stops, the original signal *S(t)*, can be represented as

$$S(t) = \sum_{k=1}^{n} c_k + r_{final} \qquad (5.12)$$

where *n* is the number of IMFs, c_k the *k*th IMF and r_{final} is the final residue, which is estimated in the step (9).

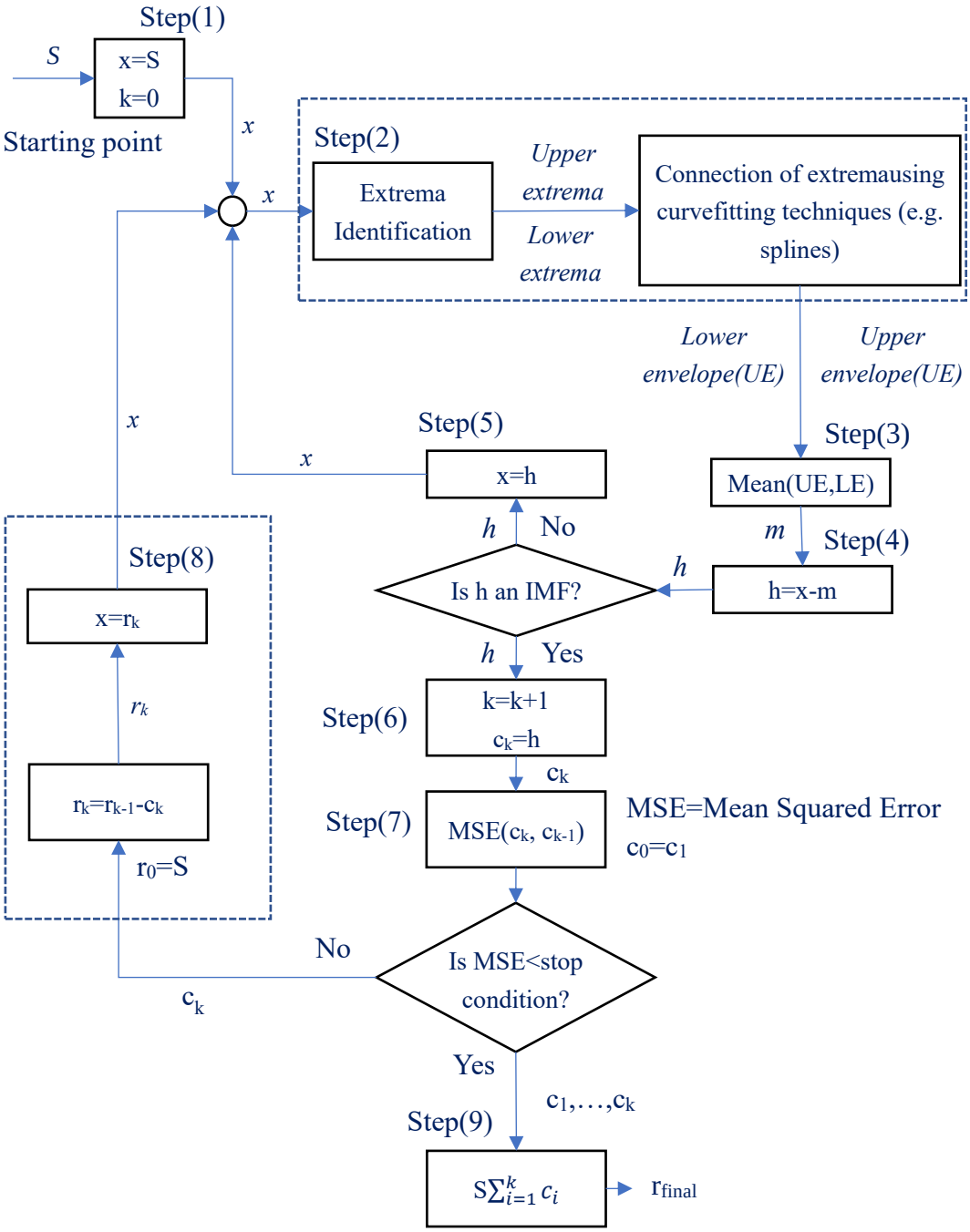

Figure 5.4 Block diagram of empirical mode decomposition showing the sequence of steps required for the estimation of intrinsic mode functions.

Equation 5.12 indicates that IMFs can be linearly combined in order to obtain the decomposed signal *S(t)*. The filtering procedure that is proposed takes into account this property of the decomposition in order to filter signals. This process is stated in the next sections.

Figure 5.5 shows examples of upper, lower and mean envelopes for two arbitrary time-series, *y1* and *y2*. *y1* is a random signal, whereas *y2* is a single sinusoidal waveform oscillating at 10Hz. As the mean envelope obtained from the upper and lower envelopes of y_1 is different from zero, y_1 does not satisfy the conditions imposed by the definition of IMFs so it is not an IMF. Therefore, the sifting process described above could be employed for the estimation of IMFs in this signal. However, *y2* satisfies the definition of IMFs, and thus is an IMF already.

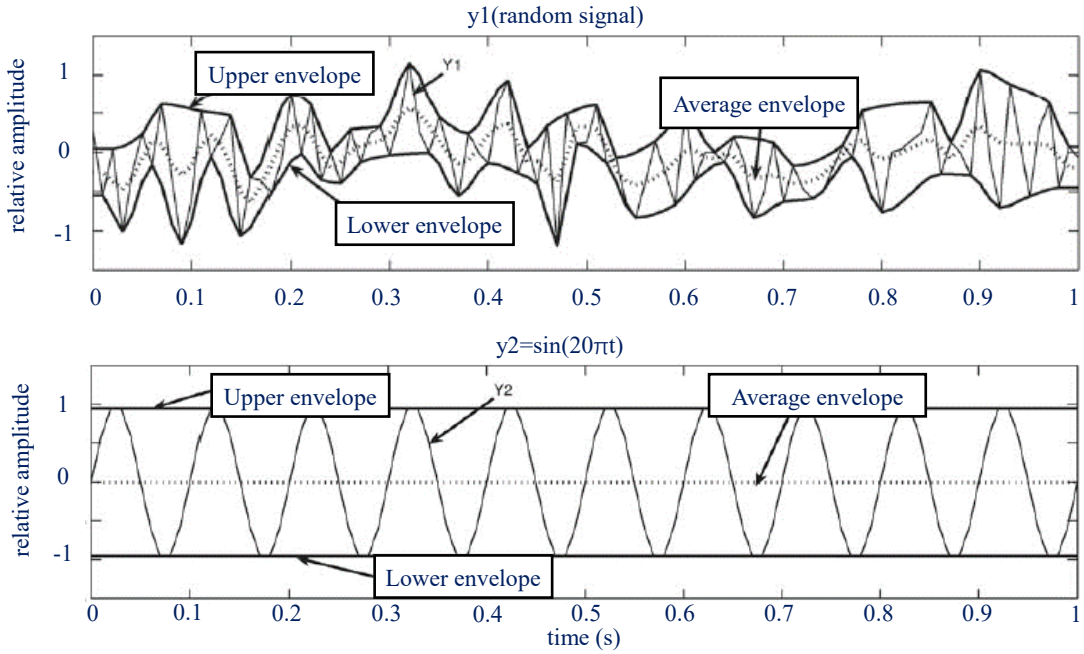

Figure 5.5 Examples of upper, lower and mean envelope for two distinct time-series. *y1* is a random signal, *y2* is a sine wave oscillating at 10Hz and *t* is time in seconds. Note that *y1* is not an IMF as its mean envelope is not zero, and that *y2* is an IMF.

5.2.2 The algorithm for signal filtering based on the EMD

The process of noise removal is based on the fact that it is possible to filter signal components individually instead of filtering the original signal. It's desirable because some components may strengthen the noise and thus it's easier to weaken the signal.

Similarly, the empirical mode decomposition also provides the decomposition of a signal into different time-scales. So it is also possible to filter signal components

individually instead of the original signal. It suggests that the strategy for signal de-noising may also be applied to intrinsic mode functions. Thus, the procedures for EMD are stated as following:

1. Decompose the signal into IMFs.

2. Threshold the estimated IMFs.

3. Reconstruct the signal.

This procedure is practical, mainly due to the empirical nature of the EMD method, and it may be applied to any signal as the EMD does not make any assumption about the input time-series. A block diagram describing the steps for its application is shown in Figure 5.6. First, the EMD method is used for decomposing the input signal into intrinsic mode functions, IMF_1,.., IMF_N, where N is the number of IMFs. These IMFs are then soft-thresholded, yielding tIMF$_1$,..., tIMF$_N$, which are thresholded versions of the original components. The filtered signal is obtained as a linear summation of thresholded IMFs.

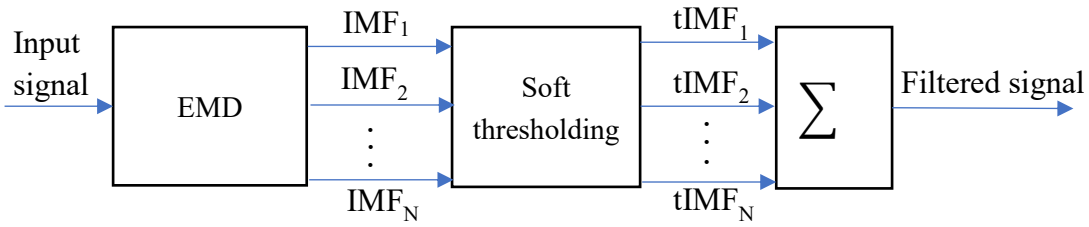

Figure 5.6 The EMD method is employed for decomposing the input signal into IMFs, which are soft-thresholded.

A very common strategy used in the filtering procedure based on wavelets is to use the soft-thresholding technique described by Donoho [96], i.e. first the signal is decomposed by means of wavelets and the detail coefficients resulting from this

decomposition are thresholded through soft-thresholding, and then employed for reconstruction of the filtered signal.

A similar idea is used for thresholding IMFs. For each IMF from 1 to *N* a threshold, t_n, n=1,...,N, is selected and soft-thresholding (defined in Equation 5.13) is applied to individual IMFs as shown in Equation 5.13,

$$tIMF_n = sign\left(IMF_n\right)\left(\left|IMF_n\right| - t_n\right)_+ \qquad (5.13)$$

where $t\text{IMF}_n$ is the de-noised version of the *n*th IMF and the function $(x)_+$ is defined as

$$\left(x\right)_+ = \begin{cases} 0, x < 0 \\ x, x \geq 0. \end{cases} \qquad (5.14)$$

The threshold t_n is estimated by using the following strategy: a window of noise is selected from the original signal and then the boundaries of this window are used to extract a region of noise from IMFs. The standard deviation of each region is then estimated and regarded as the required thresholds.

5.3 Conclusions

In this chapter, two kinds of filters are introduced, which are wavelet decomposition and empirical mode decomposition, the theoretical formulas are deduced, and the detailed steps of signal processing are proposed.

While EMD and wavelets are all used to decompose signals, EMD is fundamentally different from the other. Wavelet transforms selects a set of basis signal components and then calculates the parameters for each of these signals such that their aggregate will compose the original signal. The wavelet transform uses complex and orthogonal waveforms.

On the other hand, EMD makes no assumptions a priori about the composition of the signal. Rather, it uses spline interpolation between maxima and minima to successively trace out "Intrinsic Mode Functions". Each IMF will be a single periodic oscillator, but otherwise cannot be predicted before it is empirically observed from the signal. The number of IMFs cannot be predicted. These two disadvantages can make EMD difficult to work with under certain circumstances.

Chapter 6 A modified leakage localization method using MLPNN

6.1 Modified GCC location method

Figure 6.1 presents a pressurized piping system: l is the distance between the two sensors, and l_1 and l_2 are the distances between the leak point and sensors 1 and 2, respectively.

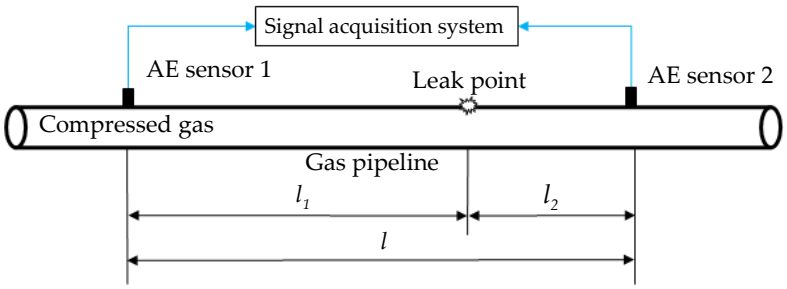

Figure 6.1 Schematic of the pressurized piping system.

If there is a leak between the two AE sensors, the two measured signals $x_1(t)$ and $x_2(t)$ can be mathematically modeled [97] as

$$\begin{aligned} x_1(t) &= h_1(t) \otimes s(t) + n_1(t), \\ x_2(t) &= h_2(t) \otimes s(t) + n_2(t), \end{aligned} \qquad (6.1)$$

where $s(t)$ is the leakage-induced signal measured at the leak location, the parameter t is the discrete-time counter, and d denotes the time delay between two measured signals. $h_1(t)$ and $h_2(t)$ are the discrete-time impulse response functions between the leak point and each sensor, respectively, and they provide the relationships between an impulse signal and each sensor signal. $n_1(t)$ and $n_2(t)$ are the background noises picked up by the two sensors, $\otimes$ is the discrete-time convolution operator. $s(t)$, $n_1(t)$ and $n_2(t)$ are assumed as stationary random signals. The noises measured by the two sensors are assumed to be mutually unrelated and unrelated with the leakage-induced signal, so the

CCF between two measured signals with noise and without noise are equivalent, and can be expressed as

$$R_{s1s2}(\tau) = R_{x1x2}(\tau), \quad (6.2)$$

where $R_{s1s2}(\tau)$ and $R_{x1x2}(\tau)$ are the CCF without noise and with noise, respectively, in terms of the time delay τ. Since the CCF is sensitive to the vibration noises[97], the time delay is commonly estimated by the GCC function [98], which can be written as

$$R_{x1x2}(\tau) = F^{-1}\left\{\Psi_g(\omega) S_{x1x2}(\omega)\right\}, \quad (6.3)$$

where $F^{-1}\{\cdot\}$ denotes the inverse discrete Fourier transform, ω denotes the frequency, and $\Psi g(\omega)$ is the frequency weighting function of the GCC function. $S_{x1x2}(\omega)$ is the CSD between two measured signals $x_1(t)$ and $x_2(t)$ [85], and can be written as

$$S_{x1x2}(\omega) = \frac{1}{2\pi}\lim_{T\to\infty} E\left[\frac{X_1^*(\omega) X_2(\omega)}{T}\right] = S_{ss}(\omega)\left|H_1^*(\omega) H_2(\omega)\right| e^{i\omega d}, \quad (6.4)$$

where $E[\cdot]$ denotes the expectation operator, $X_1(\omega)$ and $X_2(\omega)$ are the N-point discrete Fourier transforms (*DFT*) of $x_1(t)$ and $x_2(t)$, respectively, $H_1(\omega)$ and $H_2(\omega)$ are the DFT of $h_1(t)$ and $h_2(t)$, respectively, $Sss(\omega)$ is the ASD of $s(t)$, and $(\cdot)^*$ means complex conjugation. Since multiplication in the frequency domain corresponds to convolution in the time domain [99], the GCC function between two measured signals in terms of the time delay τ can be derived by substituting Equation 6.4 into Equation 6.3, and expressed as

$$R_{x1x2}(\tau) = F^{-1}\left\{S_{ss}(\omega)\Psi_g(\omega)\left|H_1^*(\omega) H_2(\omega)\right| e^{i\omega d}\right\} = R_{ll}(\tau) \otimes \psi_g(\tau) \otimes \delta(\tau + d), \quad (6.5)$$

where $\psi_g(\tau) = F^{-1}\{\Psi g(\omega)|H_1^*(\omega)H_2(\omega)|\}$, $\delta(\tau+d) = F^{-1}\{e^{i\omega d}\}$ and $R_{ll}(\tau) = F^{-1}\{Sss(\omega)\}$ is the autocorrelation function of $s(t)$. The time delay between two measured signals is equal to the quotient of the offset of the GCC maximum peak and the sampling frequency. $\delta(\tau+d)$ is a function equal to zero everywhere except for $\tau=-d$, and the Dirac Delta function's integral over the entire real line is equal to one. If $\Psi_g(\omega)=1$, the Dirac delta function $\delta(\tau+d)$ delayed by d will be broadened by $Sss(\omega)$, $H_1(\omega)$ and $H_2(\omega)$ [100]. In fact, $Sss(\omega)$ is often unknown as it depends on the leakage aperture, the gas pressure

difference between inside and outside the pipe [10], etc. However, $H_1(\omega)$ and $H_2(\omega)$ can be obtained by the impulse response method [101] and can be calculated by

$$H_i(\omega) = \frac{Y_i(\omega)}{X(\omega)}, i = 1, 2, \quad (6.6)$$

where the parameter i indicates the sensor serial number, $Y_i(\omega)$ denotes the DFT of the impulse response signal measured by the corresponding sensor, and $X(\omega)$ is the DFT of the impulse signal measured by the impact hammer. In this study, the impulse signal is assumed as the Dirac delta function. Therefore, to compensate for the weakening effect of the pipes on the AE signals, the modified frequency weighting function of the GCC function is written as

$$\Psi_g(\omega) = \frac{1}{\left|H_1^*(\omega) H_2(\omega)\right|}, \quad (6.7)$$

The modified GCC function $R_{x1x2}^g(\tau)$ can be derived by substituting Equation 6.4 and Equation 6.7 into Equation 6.3 and expressed as

$$R_{x1x2}^g(\tau) = F^{-1}\left\{S_{ss}(\omega) e^{i\omega d}\right\} = R_{ll}(\tau) \otimes \delta(\tau + d). \quad (6.8)$$

Compared with Equation 6.5, pre-filter $\Psi_g(\omega)$ removes the effects of the propagation paths on the AE signal, $\delta(\tau+d)$ is only broadened by $S_{ss}(\omega)$. Therefore, the modified frequency weighting function can increase the degree of correlation between two measured signals and improve the accuracy of the time delay estimation. The modified frequency weighting function differs from the PHAT processor function [100] in that the frequency weighting function involves pre-whitening of the leakage-induced signal. To reduce the effects of noise on the time delay estimation, only the leakage-induced signal with greater power spectral density should be extracted and processed by the proposed pre-filter.

Figure 6.2 shows a schematic of the modified GCC location method, which contains N-point DFT, complex conjugate, cross power spectrum, pre-filter and N-point inverse discrete Fourier transform (IDFT).

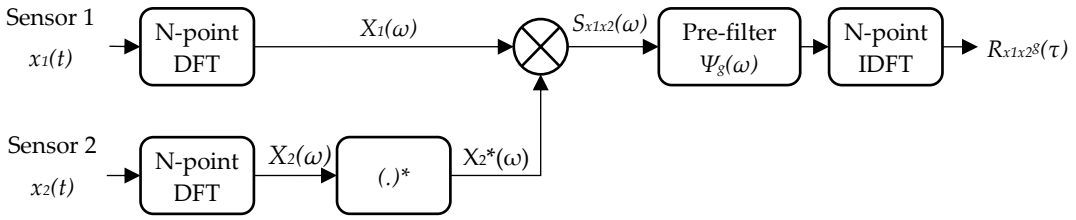

Figure 6.2 Schematic of the implementation of the modified GCC location method.

The leakage can be located by

$$l_{est} = \frac{l + v(\omega_0) d_{est}}{2}, \qquad (6.9)$$

where l is the distance between the two sensors, l_{est} is the estimated distance between the leak and one sensor, and d_{est} is the time delay estimation. The frequency-dependent speed $v(\omega_0)$ [9] of AE signals along the pipe wall is discussed. In this study, the relative location error with respect to the distance between the leak and one sensor is determined as

$$\delta l = \frac{|l_1 - l_{est}|}{l_1} \times 100\%. \qquad (6.10)$$

6.2 MLPNN classifier

The mathematical model of the biological neural network is defined as the artificial neural network [102]. The relationships between the input and output vectors can be obtained after the artificial neural networks are trained. A neural network can be applied to solve nonlinear problems, MLPNN is a commonly used model. Figure 6.3 shows the MLPNN with three layers. The input and output layers accept the external input vectors in the learning mode. Every neuron in the input and hidden layers connects to every neuron in the hidden and output layers, respectively. The input layer L_1 is comprised of P variables $x=[x_1, \cdots, x_P]^T$, which are processed by the following equation

$$a_j = \sum_{i=1}^{P} \omega_{ij}^{(1)} x_i + \omega_0^{(1)},\ j = 1, \cdots, M, \qquad (6.11)$$

where M is the number of neurons in the hidden layer, and the superscript indicates that the parameter $\omega_{ij}^{(1)}$ is the connection weight between the neuron x_i in the input layer L_1 and the neuron z_j in the hidden layer L_2. The parameter $\omega_0^{(1)}$ represents the bias of the variable a_j, which prevents a_j from becoming zero. Then a_j is transformed by an activation function, which is the logistic sigmoid function in this study, and it is given by

$$z_j = f\left(a_j\right) = \frac{1}{1+e^{-aj}}. \qquad (6.12)$$

Similarly, the neuron y in the output layer L_3 receives the variables z_j as shown in the following equation

$$y = \sum_{j=1}^{M} \omega_j^{(2)} z_j + \omega_0^{(2)}, \qquad (6.13)$$

where $\omega_j^{(2)}$ and $\omega_0^{(2)}$ are the connection weight and the bias in the hidden layer, respectively. For the regression problem, the aim of the training process is to minimize the error function as shown in the following equation by the gradient descent method

$$E\left(\omega\right) = \frac{\left|y\left(\omega\right) - d\right|^2}{2}, \qquad (6.14)$$

where d is the distance between the vibration source and one sensor, ω is the set of all weights and biases, and $y(\omega)$ represents the neuron in the output layer. All the weights and biases need to be updated by training the MLPNN on labeled data until the error function becomes small enough or the maximum iteration is reached; then the MLPNN can be used as a leakage locator.

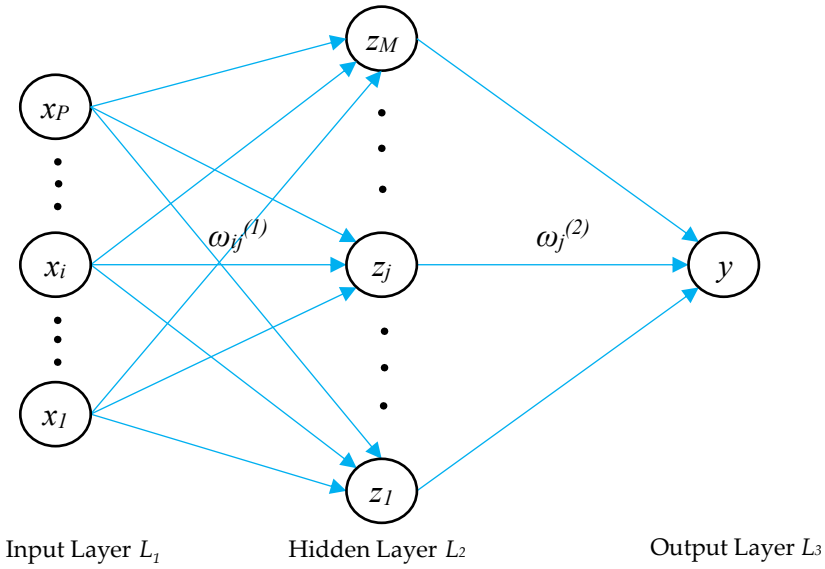

Figure 6.3 The MLPNN with input, hidden, and output layers.

6.3 Signal processing for leakage location

The leakage location procedure for the MLPNN locator is shown in Figure 6.4, and the MLPNN locator operates in two different modes:

1. In the learning mode, the training sets of the MLPNN contain the input vectors and the output vectors. The input vectors are the energy ratios of two impulse response signals in corresponding frequency bands. Since the impulse response signals are non-stationary signals, and the wavelet packet analysis is suitable for processing the non-stationary signals, then the impulse response signals were processed by the wavelet packet transform in this study. The output vectors are the distances between one sensor and each impact location. The learning procedure for the MLPNN is as follows:

Since the energy of leakage-induced signal at frequency band from 100 kHz to 150kHz is higher than at other frequency bands, and three level decomposition can extract the signal in this frequency range, so all the impulse response signals are

decomposed into three layers wavelet packet coefficients, reconstruct the signals in eight frequency bands by wavelet packet coefficients. The Haar wavelet is used in this study.

(2) Calculate the energies of the decomposed signals in step 1; then calculate the energy ratios of two impulse response signals in the corresponding frequency band.

(3) Train the MLPNN with the input and output vectors. The input vectors are the energy ratios in step 2, and the output vectors are the distances between one sensor and each impact location, and the epochs the training method is set to 0.01.

2. In the application mode, the trained MLPNN locator can locate the leak by using the energy ratios of the leakage-induced signals in the frequency bands with greater power spectral density. The leakage location procedures for the MLPNN locator are described as follows:

(1) Measure the leakage-induced signals by using the two AE sensors.

(2) Determine the peak frequency of the leakage-induced signals by using the power spectral density.

(3) Estimate the group speed of the leakage-induced signals by using the peak frequency in step 2 and the known group speed dispersive curve of the fundamental flexural mode.

(4) Calculate the CCC by using the CCF method and the modified GCC method.

(5) Compare the maximum peak amplitudes of the two CCCs obtained in step 4. $\rho_{x1x2}{}^{c}$ and $\rho_{x1x2}{}^{g}$ are the maximum peak amplitudes of the CCCs obtained by using the CCF method and the modified GCC method, respectively. When $\rho_{x1x2}{}^{g}$ is greater than $\rho_{x1x2}{}^{c}$, it implies that compared to the CCC obtained by using CCF method, the CCC

obtained by using modified GCC method is more reliable; then perform step 6, otherwise perform step 7.

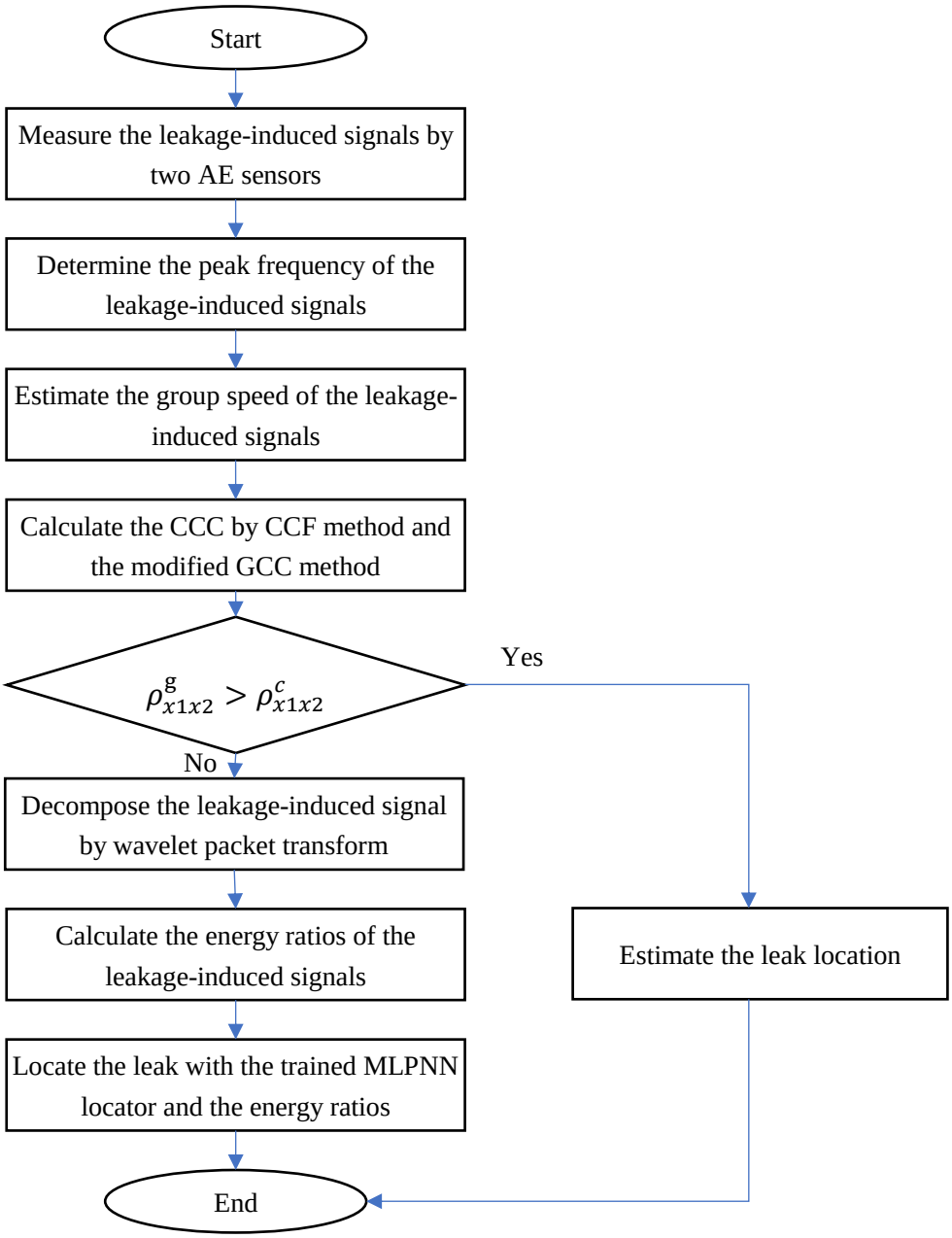

Figure 6.4 Flowchart of the leakage location method for the MLPNN locator.

(6) Calculate the distance between the leakage and sensor 1 by Equation 6.9. The group speed of the leakage-induced signal was determined in step 3, and the time delay was determined by the sampling frequency and the offset of the CCC maximum peak obtained by the modified GCC method in step 4.

(7) Decompose the leakage-induced signals into three layers wavelet packet coefficients, reconstruct the signals in eight frequency bands by using the wavelet packet coefficients.

(8) Calculate the energy ratios of the decomposed signals in the frequency bands with the greater power spectral density.

(9) Locate the leakage by using the energy ratios in step 8 and the trained MLPNN locator.

6.4 Conclusions

This chapter proposed a leakage location method using the modified GCC location method in combination with the attenuation-based location method using MLPNN. The GCC location method can compensate for the weakening effect of the different propagation paths on the leakage-induced signals, it also can increase the degree of the correlation between two measured signals and improve the accuracy of the time delay estimation. Unlike the CCF location method, the MLPNN locator locates a leak not only by the time delay estimation between two measured signals but also by the energy ratios of two leakage-induced signals measured by two sensors in the frequency bands with greater power spectral density. In addition, the wave speed was determined more accurately by using the peak frequency in combination with the group speed dispersive curve of the fundamental flexural mode.

Chapter 7 Laboratory experiments

7.1 Experimental setup and data collection

The experimental setup consists of two parts: a pressurized piping system and a signal acquisition system, as shown in Figure 7.1. If the gas pressure in the pipe is too low, the energy of the leak-induced signal will be small, then the leak-induced signal will be difficult to detect. Therefore, in the pressurized piping system, an air compressor (NH-5, Hanshin product) supplies 7 bar gas pressure to a 15m-long steel pipe (ASTM A 312 TP304) with a pipe wall thickness and external diameter of 2.8 mm and 33.4 mm, respectively. One end of the pipe was blocked, and the other end was connected to the air compressor via a hose. To avoid the air compressor vibration noise affecting the experimental results, the air compressor was placed far away from the piping system. The pipe was supported by a sponge material to reduce energy dissipation of the AE signal on the pipe wall to the ground. The diameter of the leakage orifice in the early stage of pipeline leakage is usually small. To verify the proposed method can locate a leak in the early stage of pipeline leakage, the simulated leak orifice with a diameter of 0.3 mm was punched in the pipe wall. The simulated leak source, the AE sensor mounted on the pipe wall, an impulse hammer and the placement of two AE sensors along the pipe are shown in Figures 7.2, 7.3, 7.4 and 7.5, respectively. The pipe wall had been cleaned with sandpaper before the AE sensors were mounted with the magnetic hold downs and vacuum grease couplant.

The signal acquisition system consists of two R15a sensors with a resonant frequency of 150 kHz, an impulse hammer (086C03), a data acquisition card (USB-5132, NI product) and a personal computer (PC) equipped with NI-SCOPE software. Since the sensitivity of the AE sensors is high in the frequency range between 50 kHz and 400 kHz, data were captured at a sampling rate of 800 kHz in the experiment.

Analog to digital conversion was performed by the data acquisition card connected to the PC. Data were recorded into the PC for the signal processing and preprocessed by the NI-SCOPE software, including the preamplification and anti-aliasing filtering.

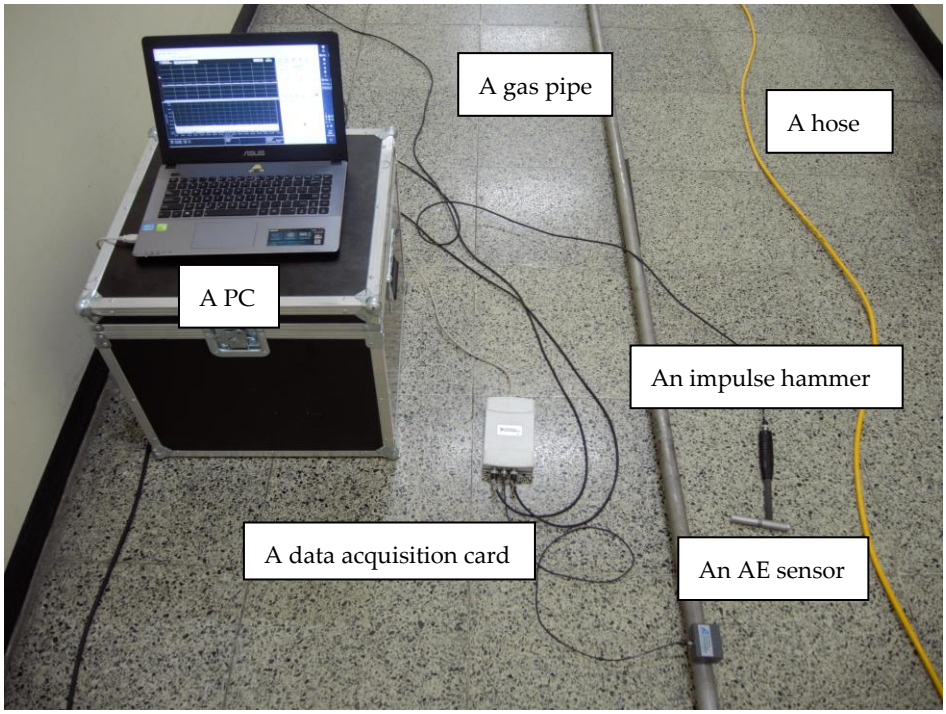

Figure 7.1 Experiment system diagram: (i) a gas pipe, (ii) two AE sensors, (iii) an impulse hammer, (iv) a data acquisition card, (v) a PC, and (vi) a hose.

Figure 7.2 A simulated leak orifice of the pipe.

Figure 7.3 The AE sensor mounted with the magnetic hold down and vacuum grease couplant.

Figure 7.4 An impulse hammer.

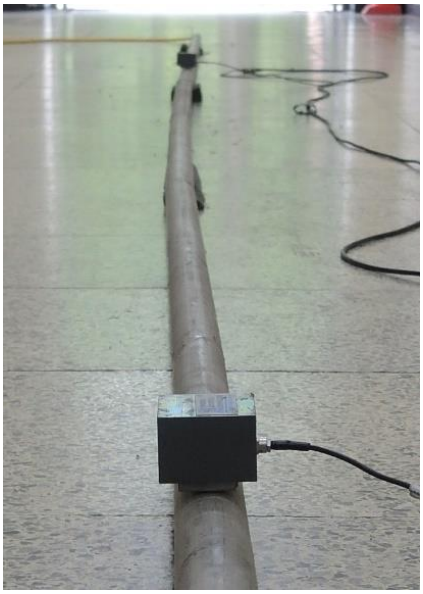

Figure 7.5 The placement of two AE sensors along the pipe.

In the experiment, the training sets for MLPNN include the distances between one sensor and each impact location and the impulse response signals energy ratios between two sensor signals in different frequency bands. The impulse signal is measured by the sensor in the impact hammer, and the impulse response signals were measured by AE sensors when the pipe was tapped by the impact hammer, and the tapping locations were distributed along a straight line between the two AE sensors. To avoid the simulated leak orifice affecting the impulse response signal, the impact test was performed before the simulated leak orifice was punched. The impulse response signals were measured by AE sensors when the pipe was tapped by the impact hammer, and the tapping locations were distributed along a straight line between the two AE sensors. The test sets for MLPNN were the energy ratios of leakage-induced signals in different frequency bands. The leakage-induced signals were generated by the friction force between the jet of the leaking gas and the simulated leak orifice.

7.2 Characteristics of the frequency domain

Figure 7.6 shows the power spectral densities of the leakage-induced signals collected at the distances of 1 m and 2 m away from the simulated leak source. The center frequency of the leak-induced signal is proportional to the gas jet velocity and inversely proportional to the leakage aperture [10], and it's also related to the resonant frequency of the sensor and the propagation distance between the leak and the sensor. It's can be seen in Figure 7.6 that the maximum amount of leakage-induced signal energy occurs in frequencies near 124 kHz. The amplitude of the power spectral density decreases with increasing propagation distance. Since the peak frequency of leakage-induced signals is 124 kHz, the wave speed can be determined to be 2404 m/s by the peak frequency in combination with the known group speed dispersive curve of the fundamental flexural mode.

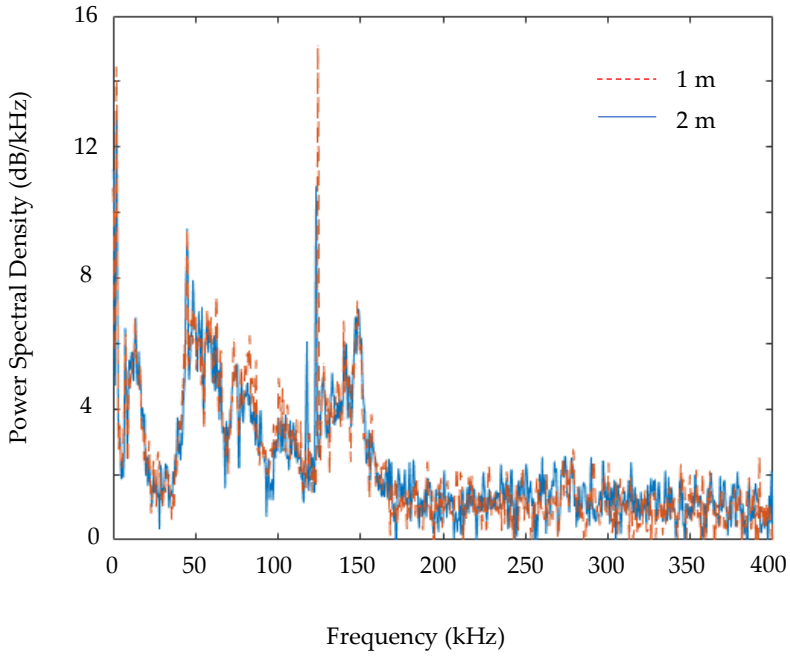

Figure 7.6 Comparison of the power spectral densities of the leakage-induced signal in the different distances (L_1=1 m, 2 m) away from the leak source.

7.3 Characteristics of the signal energy ratios

To verify the consistency of weakening the effect of the pipe on two kinds of signals, which are the impulse response signals and leakage-induced signals measured by maintaining a distance of 14 m between the two sensors while varying the distance between sensor 1 and the simulated leak orifice. Since the maximum amount of leakage-induced signal energy occurs in frequencies near 124 kHz, the signal-to-noise ratio at this frequency band is higher than at other bands, the impulse response signal in frequencies near 124 kHz was also extracted with wavelet packet transform, and the signal energy ratios between the two sensors were calculated. Figure 7.7 shows the fitting curves of the signal energy ratios as a function of the propagation distance. The horizontal axis denotes the distance between sensor 1 and the simulated leak orifice. The vertical axis denotes the energy ratios of the leakage-induced signal and the impulse

signal measured by the two sensors. The difference between the two fitting curves is small, which implies that the weakening effect of the pipe on the AE signals is proportional to the propagation distance, irrespective of any leakage-induced signals or impulse response signals. Therefore, the signal energy ratio can also be used to locate the vibration excitation source.

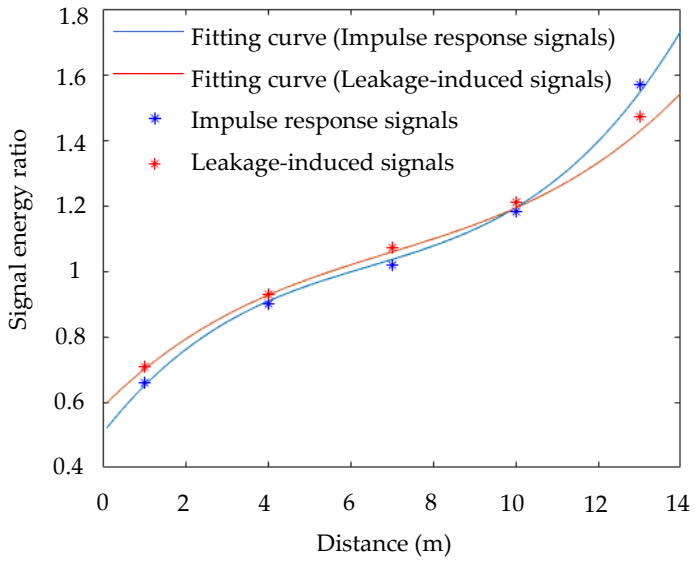

Figure 7.7 Fitting curves of the signal energy ratios of the AE signals measured by the two sensors.

7.4 Characteristics of the time domain

Figures 7.8a and 7.8b show the impulse response signals collected at distances of 0.4 m and 13 m away from the impact location, respectively. The maximum amplitude of the impulse response signals decreases as the propagation distance increases, which indicates that the energy of the impulse response signal decreases due to energy attenuation. Moreover, the closer the vibration source is to the sensor, the earlier the impulse response signal begins to oscillate.

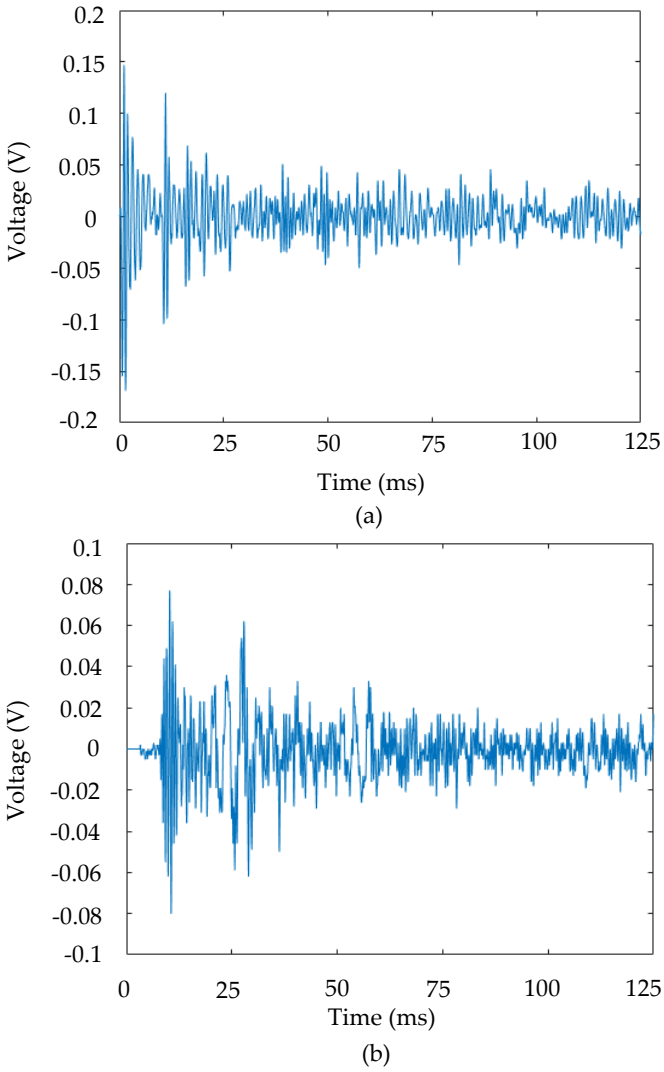

Figure 7.8 Impulse response signals acquired at different distances from sensor 1: (a) 0.4m and (b) 13m.

Figures 7.9a and 7.9b show the CCC obtained by the CCF method and the modified GCC method, respectively. The time delay estimation only depends on the shift value of the maximum peak in cross-correlation coefficient with respect to the central point, and it can be calculated as the product between the sampling period and the shift of the CCF maximum peak. Two maximum peaks can be observed, and the time delay estimations are -0.00020 seconds and -0.00034 seconds, respectively. The distance estimations between the leak and sensor 1 are 1.83 m and 1.99 m, respectively. Since the relative location error in this study is equal to the quotient of leakage location

error and the distance between the leak and sensor 1, and the real distance between the simulated leak orifice and sensor 1 is 2.16 m, so the relative location errors are 15% and 8%, respectively. The maximum peak amplitudes of the two CCCs are 0.168 and 0.236, respectively. Hence, the modified pre-filter can improve the accuracy of the time delay estimation and increase the degree of the correlation between the two measured signals.

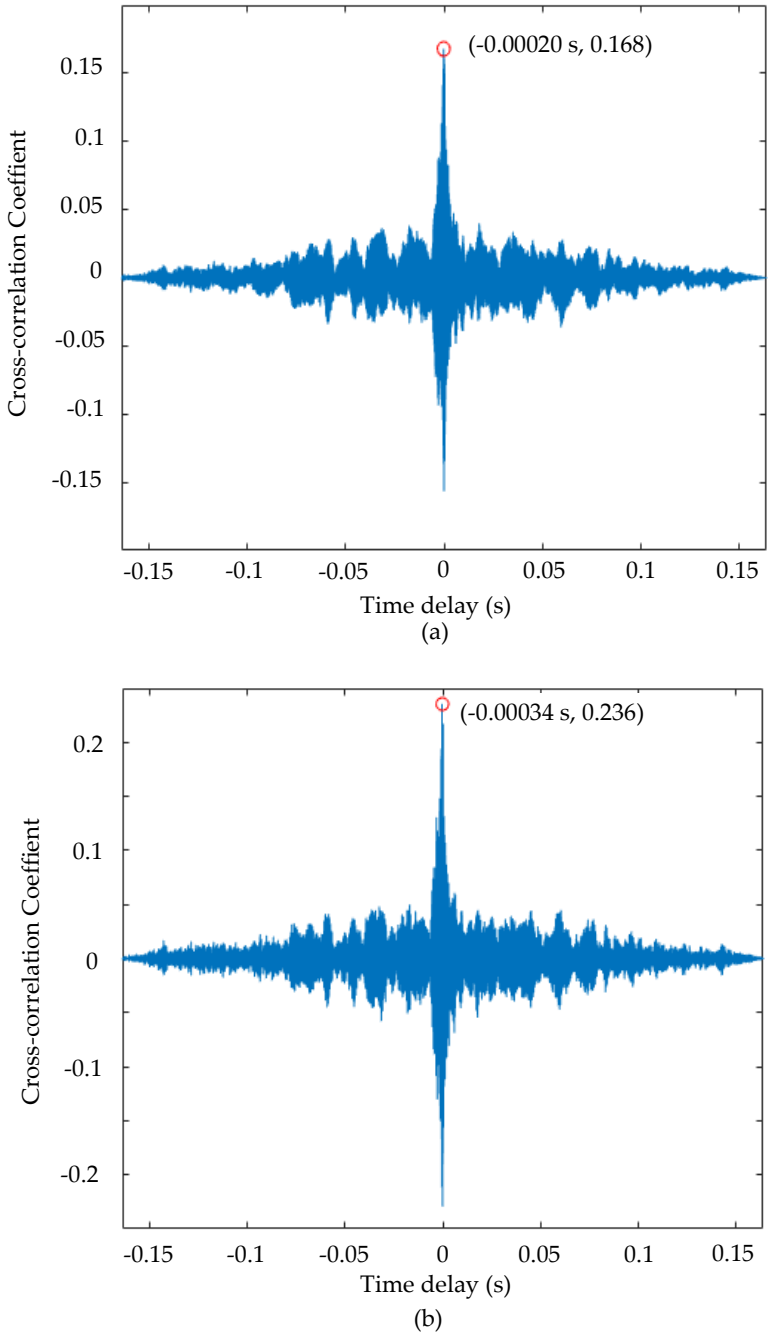

Figure 7.9 Cross-correlation coefficients (CCCs) obtained by two methods: (a) CCF location method (b) modified GCC location method.

7.5 Leakage location analysis

To verify the reliability of the MLPNN locator, the gas leakage was located by the CCF location method and the MLPNN locator under different conditions, which are maintaining a distance of 2.16 m between the simulated leak orifice and sensor 1 and varying the distance (1.08 m, 2.36 m and 3.54 m) between the simulated leak orifice and sensor 1. In addition, the group speed of the leakage-induced signal was determined by the peak frequency of the leakage-induced signal and the group speed dispersive curve of the fundamental flexural mode. Tables 7.1 and 7.2 show the location results obtained by the CCF method and the MLPNN locator. The relative location errors in Table 7.2 show that the relative location errors increase as the distance between the two sensors increases, which implies that some high-frequency components of the leakage-induced signal attenuate as the propagation distance increases. Tables 7.2 and 7.3 show the location results obtained by the MLPNN locator in different gas pressure. The lower the air pressure, the greater the locationing error. This is because the high-frequency components of the leak-induced signal was weakened and disappeared before the sensors detected them.

Figures 7.10a and 7.10b show the histograms of the relative location errors in Tables 7.1 and 7.2, respectively. The vertical axis represents the number of measurements, and the horizontal axis represents the percentage of relative location error. These two tables show the measurement results of twelve groups by using the proposed method and the CCF respectively, so the total number of measurements Figures 7.10a and 7.10b both are twelve. Although the sample size is somewhat small, all the measurement results are typical, they can show the location accuracy of two

location methods. The averages of the relative location errors are 18% and 4%, respectively, which indicates that the average of the relative location errors obtained by the MLPNN locator is reduced by 14% compared to that using the CCF location method. Consequently, the MLPNN locator is more suitable for locating a leak in a gas pipe than the CCF location method is. However, the MLPNN locator suffers the drawback of needing to be trained again if one of the following experimental conditions changes: for example, the distance between the two AE sensors, the geometric parameters of the pipe wall, or the material of the pipe wall.

Table 7.1 The location results obtained by the CCF location method.

$L(m)$	3.24	3.24	3.24	3.24	4.52	4.52	4.52	4.52	5.70	5.70	5.70	5.70
$f(kHz)$	124.2	123.8	123.4	125.4	105.5	103.4	107.2	106.7	104.7	104.3	104.7	103.5
$v(m/s)$	2404	2400	2397	2415	2200	2173	2222	2215	2190	2186	2190	2175
$l_1(m)$	2.16	2.16	2.16	2.16	2.16	2.16	2.16	2.16	2.16	2.16	2.16	2.16
$\hat{l}_1(m)$	1.78	1.71	1.82	1.72	1.70	1.77	1.75	1.79	1.83	1.74	1.79	1.83
$\Delta l_1(m)$	0.38	0.45	0.34	0.44	0.46	0.39	0.41	0.37	0.33	0.42	0.37	0.33
$\delta l_1(\%)$	17.6	20.1	15.7	20.4	21.3	18.1	19.0	17.1	15.3	19.4	17.1	15.3

L is the distance between the two AE sensors,
f is the peak frequency of the leakage-induced signal,
v is the group speed estimation of the leakage-induced signal,
l_1 is the real distance between the leak and sensor 1,
$\hat{l}_1$ is the distance estimation between the leak and sensor 1,
Δl_1 is the leakage location error,
δl_1 is the relative location error.

Table 7.2 The location results obtained by the MLPNN locator(gas pressure=7bar).

$L(m)$	3.24	3.24	3.24	3.24	4.52	4.52	4.52	4.52	5.70	5.70	5.70	5.70
$f(kHz)$	124.2	123.8	123.4	125.4	105.5	103.4	107.2	106.7	104.7	104.3	104.7	103.5
$v(m/s)$	2404	2400	2397	2415	2200	2173	2222	2215	2190	2186	2190	2175
$l_1(m)$	2.16	2.16	2.16	2.16	2.16	2.16	2.16	2.16	2.16	2.16	2.16	2.16
$\hat{l}_1(m)$	2.19	2.18	2.20	2.25	2.26	2.09	2.25	2.27	1.99	2.23	2.28	1.98
$\Delta l_1(m)$	0.03	0.02	0.04	0.09	0.10	0.07	0.09	0.11	0.17	0.07	0.12	0.18
$\delta l_1(\%)$	1.4	0.9	1.9	4.2	4.6	3.2	4.2	5.1	7.9	3.2	5.6	8.3

Table 7.3 The location results obtained by the MLPNN locator(gas pressure=3.5bar).

$L(m)$	3.24	3.24	3.24	3.24	4.52	4.52	4.52	4.52	5.70	5.70	5.70	5.70
$f(kHz)$	114.3	113.2	113.8	115.4	95.4	93.3	97.6	96.9	84.7	86.3	84.8	83.1
$v(m/s)$	2302	2287	2300	2319	2059	2025	2092	2081	1873	1877	1876	1843
$l_1(m)$	2.16	2.16	2.16	2.16	2.16	2.16	2.16	2.16	2.16	2.16	2.16	2.16
$\hat{l}_1(m)$	2.23	2.24	2.21	2.10	2.02	2.02	2.32	2.33	1.95	2.36	2.37	2.35
$\Delta l_1(m)$	0.07	0.08	0.05	0.06	0.14	0.14	0.16	0.17	0.21	0.20	0.21	0.19
$\delta l_1(\%)$	3.2	3.9	2.3	2.9	6.6	6.4	7.4	7.8	9.9	9.2	9.8	9.0

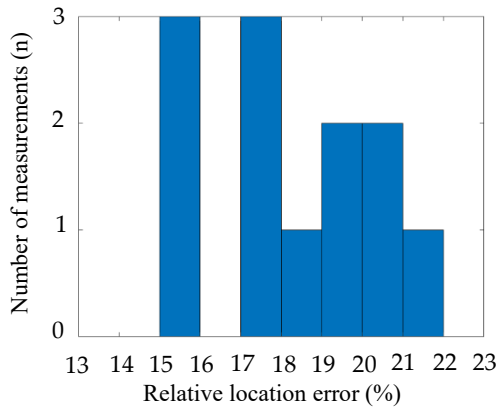

(a)

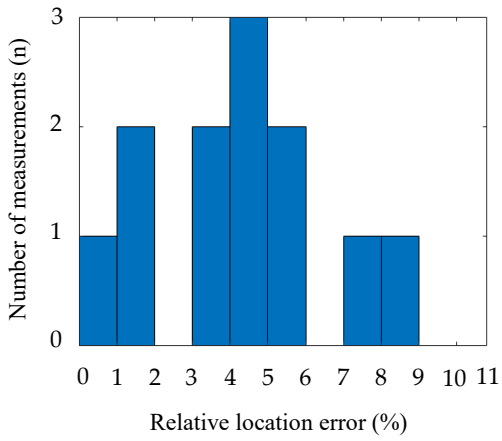

(b)

Figure 7.10 Histograms of the relative location errors obtained by two methods: (a) CCF location method and (b) MLPNN locator.

7.6 Conclusions

Leak-induced signals measured in-situ are analyzed based on the proposed method in this chapter, and the MLPNN locator was experimentally verified. The average of the relative location errors obtained by the MLPNN locator was reduced by 14% compared to that using the CCF location method. Hence, the MLPNN locator is more suitable for locating a leak in a gas pipe than the CCF location method is.

There are two reasons for the improved location accuracy, the first one is that the

GCC location method can increase the degree of the correlation between two measured signals and improve the accuracy of the time delay estimation; the second one is that the speed of the AE signal is online estimated by the peak frequency of the AE signal in combination with the known group speed dispersive curve of the fundamental flexural mode, and only the leakage-induced signal with greater power spectral density should be extracted and processed by the proposed pre-filter for reducing the effects of noise on the time delay estimation.

Chapter 8 Conclusions

Pipelines are used extensively to transport and distribute natural gas and other easy-flowing products, pipe leakage is a common phenomenon in the continuous transportation process. Guided waves will be generated in pipes due to the leakage on the pipe wall. The guided wave in the pipe is divided into longitudinal mode, torsional mode and flexural mode. The three-dimensional displacement vector and the group velocity dispersion curve of the guided wave in a pipe can be derived based on the Navier displacement motion equation and known boundary conditions for the given pipe. The influence of the wall thickness and diameter on the dispersion curve of the guided wave in a pipe is proposed, and the phase velocity dispersive curves of the guided wave in different cases are obtained by MATLAB program. It is can be seen that the larger the a/h ratio, the lower the cutoff frequency of the guided wave in a pipe.

Due to limited knowledge of the characteristics of leak-induced signals in pipes, cross-correlation method is difficult to employ in pipes. Some parameters require optimization when a leak between two sensors is located. The maximum value of time delay which can be measured is limited by the length of FFT. Various time-delay estimators used in GCC are compared for leakage detection in pipes. It has been shown that PHAT, SCOT and ML estimators have the desirable feature of sharpening the CCF peak. The PHAT estimator is designed to give a delta function, the SCOT and ML estimators additionally take account of the effect of background noise in the estimation procedure. However, the ML estimator has the effect of overemphasizing or underemphasizing at certain frequencies.

Velocity and attenuation of leak-induced signals with distance play an important role in locating a leak. Wave velocity can be approximated by the analytical method, time-of-flight method, cross-correlation method, three sensors methods and phase-frequency method. These methods require prior knowledge of the pipe physical properties and a known leak-induced signal/transient event source, and the discontinuities in the pipe will affect the wave velocity.

In addition, these methods don't consider the dispersion characteristics of the AE signal, a new method based on the dispersion characteristics of the AE signal is proposed. The AE signal group velocity changes with the frequency due to the dispersion characteristics of the AE wave group velocity, then the speed of the AE signal can be online estimated by the peak frequency of the AE signal in combination with the known group speed dispersive curve of the fundamental flexural mode. This method for determining the wave velocity can effectively eliminate the effects of noise, so it's used to determine the AE signal velocity in this study.

This paper proposed a new leakage location method using the modified GCC location method in combination with the attenuation-based location method using MLPNN. The GCC location method can compensate for the weakening effect of the different propagation paths on the leakage-induced signals, it also can increase the degree of the correlation between two measured signals and improve the accuracy of the time delay estimation. Unlike the CCF location method, the MLPNN locator locates a leak not only by the time delay estimation between two measured signals but also by the energy ratios of two leakage-induced signals measured by two sensors in the frequency bands with greater power spectral density. In addition, the wave speed was

determined by using the peak frequency in combination with the group speed dispersive curve of the fundamental flexural mode. Then leak-induced signals measured in-situ are analyzed based on the proposed method, and the MLPNN locator was experimentally verified by using a pressurized piping system and a signal acquisition system. The average of the relative location errors obtained by the MLPNN locator was reduced by 14% compared to that using the CCF location method. Hence, the MLPNN locator is more suitable for locating a leak in a gas pipe than the CCF location method is.

There are two reasons for the improved location accuracy, the first one is that the GCC location method can increase the degree of the correlation between two measured signals and improve the accuracy of the time delay estimation; the second one is that the speed of the AE signal is online estimated by the peak frequency of the AE signal in combination with the known group speed dispersive curve of the fundamental flexural mode, and only the leakage-induced signal with greater power spectral density should be extracted and processed by the proposed pre-filter for reducing the effects of noise on the time delay estimation.

REFERENCES

1. K. Edalati, N. Rastkhah, A. Kermani, M. Seiedi, A. Movafeghi, "The use of radiography for thickness measurement and corrosion monitoring in pipes", Int J Pres Ves Pip 83(10), 736-741, 2006.
2. W. Liang, J. Hu, L. Zhang, C. Guo, W. Lin, "Assessing and classifying risk of pipeline third-party interference based on fault tree and SOM", Eng Appl Artif Intel 25(3), 594-608, 2012.
3. B. Vargas-Arista, J.M. Hallen, A. Albiter, "Effect of artificial aging on the microstructure of weldment on API 5L X-52 steel pipe", Mater Charact 58(8-9), 721-729, 2007.
4. I.m.N. Ferraz, A.C.B. Garcia, F.v.C. Bernardini, "Artificial Neural Networks Ensemble Used for Pipeline Leak Detection Systems", (48579), 739-747, 2008.
5. A. Nehorai, B. Porat, E. Paldi, "Detection and Localization of Vapor-Emitting Sources", Ieee T Signal Proces 43(1), 243-253, 1995.
6. Q. Xiao, J. Li, Z. Bai, et al., "A Small Leak Detection Method Based on VMD Adaptive De-Noising and Ambiguity Correlation Classification Intended for Natural Gas Pipelines", Sensors (Basel) 16(12), 2016.
7. V.A. Faerman, A.G. Cheremnov, V.V. Avramchuk, E.E. Luneva, "Prospects of Frequency-Time Correlation Analysis for Detecting Pipeline Leaks by Acoustic Emission Method", IOP Conference Series: Earth and Environmental Science 21, 012041, 2014.
8. R.R.R. Lance E. Rewerts, and M. Amanda Clark, "Dispersion compensation in acoustic emission pipeline leak location", Review of Progress in Quantitative Nondestructive Evaluation 16,
9. S. Li, Y. Wen, P. Li, et al., "Leak location in gas pipelines using cross-time-frequency spectrum of leakage-induced acoustic vibrations", J Sound Vib 333(17), 3889-3903, 2014.
10. S. Li, Y. Wen, P. Li, J. Yang, L. Yang, "Determination of acoustic speed for improving leak detection and location in gas pipelines", American Institute of Physics 85(2), 024901, 2014.
11. S. Davoodi, A. Mostafapour, "Modeling Acoustic Emission Signals Caused by Leakage in Pressurized Gas Pipe", J Nondestruct Eval 32(1), 67-80, 2013.
12. H. Nishino, S. Takashina, F. Uchida, M. Takemoto, K. Ono, "Modal analysis of hollow cylindrical guided waves and applications", Jpn J Appl Phys 1 40(1), 364-370, 2001.
13. I. GRABEC, "Application of correlation techniques for localization of acoustic emission sources", Ultrasonics, 1978.
14. S. Davoodi, A. Mostafapour, "Gas leak locating in steel pipe using wavelet transform and cross-correlation method", The International Journal of Advanced Manufacturing Technology 70(5-8), 1125-1135, 2013.
15. A. 0Mostafapour, S. Davoodi, "Leakage Locating in Underground High Pressure Gas Pipe by Acoustic Emission Method", J Nondestruct Eval 32(2), 113-123, 2012.
16. X.C. Yu, W. Liang, L.B. Zhang, H. Jin, J.W. Qiu, "Dual-tree complex wavelet transform and SVD based acoustic noise reduction and its application in leak detection for natural gas pipeline", Mech Syst Signal Pr 72-73, 266-285, 2016.
17. M.J. Brennan, Y. Gao, P.F. Joseph, "On the relationship between time and frequency domain methods in time delay estimation for leak detection in water distribution pipes", J Sound Vib

304(1-2), 213-223, 2007.
18. J.D. Sun, Q.Y. Xiao, J.T. Wen, Y. Zhang, "Natural gas pipeline leak aperture identification and location based on local mean decomposition analysis", Measurement 79, 147-157, 2016.
19. C. Guo, Y. Wen, P. Li, J. Wen, "Adaptive noise cancellation based on EMD in water-supply pipeline leak detection", Measurement 79, 188-197, 2016.
20. J. Yang, Y. Wen, P. Li, "Leak location using blind system identification in water distribution pipelines", J Sound Vib 310(1-2), 134-148, 2008.
21. A. Carbó-Bech, De Las Heras, Salvador A, Guardo, Alfredo, "Pipeline Leak Detection by Transient-Based Method Using MATLAB", 2017.
22. T.M. El-Shiekh, "Leak Detection Methods in Transmission Pipelines", Energy Sources, Part A: Recovery, Utilization, and Environmental Effects 32(8), 715-726, 2010.
23. S. Datta, S. Sarkar, "A review on different pipeline fault detection methods", J Loss Prevent Proc 41, 97-106, 2016.
24. G. Geiger, "PIPELINE LEAK DETECTION TECHNOLOGIES AND EMERGENCY SHUTDOWN PROTOCOLS", Proceedings of the 2014 10th International Pipeline Conference, 2014.
25. R.T.-G. E.Orduña-Reyes, "New Sensor Cable for the Detection and Location of Leaks in Pipelines for Transportation of Hydrocarbons", Journal of Applied Research and Technology 10(4), 2012.
26. S.J. A, "Sensors for detecting and locating liquid leaks", U.S. Patent 4,877,923, 1989.
27. J.-M. Henault, G. Moreau, S. Blairon, et al., "Truly Distributed Optical Fiber Sensors for Structural Health Monitoring: From the Telecommunication Optical Fiber Drawling Tower to Water Leakage Detection in Dikes and Concrete Structure Strain Monitoring", Advances in Civil Engineering 2010, 1-13, 2010.
28. A.M. Pozo, F. Perez-Ocon, O. Rabaza, "A Continuous Liquid-Level Sensor for Fuel Tanks Based on Surface Plasmon Resonance", Sensors (Basel) 16(5), 2016.
29. A.S. Ashim Mishra, "Leakage Detection using Fibre Optics Distributed Temperature Sensing", 6th Pipeline Technology Conference 2011, 2011.
30. M.Z.A. Karim, "Compensated Mass Balance Method For Oil Pipeline Leakage Detection using SCADA", International Journal of Computer Science and Security 9(6), 2015.
31. L.K. Kalubu, Shubi & Sinde, Ramadhani, "An overview of pipeline leak detection and location systems", 2014.
32. H. Jin, L.B. Zhang, W. Liang, Q.K. Ding, "Integrated leakage detection and localization model for gas pipelines based on the acoustic wave method", J Loss Prevent Proc 27, 74-88, 2014.
33. J. Ji, Y. Li, C. Liu, D. Wang, H. Jing, "Application of EMD Technology in Leakage Acoustic Characteristic Extraction of Gas-Liquid, Two-Phase Flow Pipelines", Shock Vib 2018, 1-16, 2018.
34. C.N. M, "Theoretical analysis of acoustic emission signal propagation in fluid-filled pipes", Diss. Master thesis, ELECE Dept., Ryerson University, Toronto, ON, , 2009.
35. Q. Hou, L. Ren, W. Jiao, P. Zou, G. Song, "An Improved Negative Pressure Wave Method for Natural Gas Pipeline Leak Location Using FBG Based Strain Sensor and Wavelet Transform", Math Probl Eng 2013, 1-8, 2013.
36. X. Lang, P. Li, Z. Hu, H. Ren, Y. Li, "Leak Detection and Location of Pipelines Based on LMD and Least Squares Twin Support Vector Machine", IEEE Access 5, 8659-8668, 2017.
37. L. Ni, J. Jiang, Y. Pan, "Leak location of pipelines based on transient model and PSO-SVM", J

Loss Prevent Proc 26(6), 1085-1093, 2013.
38. V.K. George Georgoulas, George Nikolakopoulos, "Acoustic emission localization on ship hull structures using a deep learning approach", JVE INTERNATIONAL LTD. VIBROENGINEERING PROCEDIA. 9, 2016.
39. J. Zhou, C.R. Rios-Soberanis, O. Adiguzel, "An Approach to Acoustic Emission Technique Applications to Evaluate Damage Mechanisms in Composite Materials", MATEC Web of Conferences 30, 2015.
40. P.W. Jingmang Xu, Boyang An , Rong Chen , Jieling Xiao, Weihai Liang and Yunhua Hou "Acoustic emission monitoring of switch rail detect based on WignerVille high-order spectrum and data mining technology", The 2017 World Congress on Advances in Structural Engineering and Mechanics, 2017.
41. G. Shen, Z. Wu, J. Zhang, Advances in Acoustic Emission Technology: Proceedings of the World Conference on Acoustic Emission–2013, Springer2014.
42. D. Eitzen, H. Wadley, "Acoustic emission: establishing the fundamentals", J Res Nat Bur Stand 89(1), 75-100, 1984.
43. K. Watanabe, D. Himmelblau, "Detection and location of a leak in a gas-transport pipeline by a new acoustic method", Aiche J 32(10), 1690-1701, 1986.
44. G. Tas, J. Loomis, H. Maris, A. Bailes Iii, L. Seiberling, "Picosecond ultrasonics study of the modification of interfacial bonding by ion implantation", Appl Phys Lett 72(18), 2235-2237, 1998.
45. H.L. Choy YS, Wang C., "Sound propagation in and low frequency noise absorption by helium-filled porous material", Journal of the Acoustical Society of America 126(6), 3008-3019, 2009.
46. L.W. Luo M, Wang J, Wang N, Chen X, Song G, "Development of a Novel Guided Wave Generation System Using a Giant Magnetostrictive Actuator for Nondestructive Evaluation", Sensors (Basel) 18(3), 2018.
47. Q.X. SHEN Gongtian, HE Renyang, XIU ChangZheng, "Theoretical Analysis and Experimental Study of Gas Pipeline Leak Acoustic Emission Signal Transmit Speed", 30th European Conference on Acoustic Emission Testing, 2012.
48. X. Niu, W. Duan, H.-P. Chen, H.R. Marques, "Excitation and propagation of torsional T(0,1) mode for guided wave testing of pipeline integrity", Measurement 131, 341-348, 2019.
49. V.H. Bahareh Zaghari, Mohamed Moshrefi-Torbati, "Dispersion Behavior of Torsional Guided Waves in a Small Diameter Steel Gas Pipe",
50. M.M. Gauthier, A.I.H. Committee, H.C.A. International, Engineered Materials Handbook, Desk Edition, Taylor & Francis1995.
51. W. Sachse, Y.H. Pao, "On the determination of phase and group velocities of dispersive waves in solids", J Appl Phys 49(8), 4320-4327, 1978.
52. H. Li, X. Liu, L. Bo, "A novel method to analysis strong dispersive overlapping lamb-wave signatures", J Vibroeng 19(1), 2017.
53. W.C. Yiming Jiang, Ying huang, and Hougui Chen, "The Application of Ultrasonic Guided Wave in Grounding Grid Corrosion Diagnosis", International Journal of Computer and Electrical Engineerin 5(3), 2013.
54. S. Yan, B. Zhang, G. Song, J. Lin, "PZT-Based Ultrasonic Guided Wave Frequency Dispersion Characteristics of Tubular Structures for Different Interfacial Boundaries", Sensors (Basel) 18(12), 2018.

55. Z.B. Yan S, Song G, Lin J, "PZT-Based Ultrasonic Guided Wave Frequency Dispersion Characteristics of Tubular Structures for Different Interfacial Boundaries", Sensors (Basel) 18(12), 2018.
56. M. Gresil, A. Poohsai, N. Chandarana, "Guided wave propagation and damage detection in composite pipes using piezoelectric sensors", Procedia Engineering 188, 148-155, 2017.
57. K. T, "Ultrasonic and Electromagnetic NDE for Structure and Material Characterization: Engineering and Biomedical Applications", CRC Press, 2016.
58. E. Maksuti, F. Bini, S. Fiorentini, et al., "Influence of wall thickness and diameter on arterial shear wave elastography: a phantom and finite element study", Phys Med Biol 62(7), 2694-2718, 2017.
59. C.A. Arora K, Engdahl E R, et al, "Encyclopedia of solid earth geophysics", Springer Science & Business Media, 2011.
60. E.P. Papadakis, "Ultrasonic attenuation caused by scattering in polycrystalline media", Physical acoustics 4 Part B (2012), 269-328,
61. W. Wu, Relevant numerical methods for mesoscale wave propagation in heterogeneous media, Université Paris-Saclay, 2018.
62. C.R. F, "Seismic wave attenuation: Energy dissipation in viscoelastic crystalline solids", Reviews in mineralogy and geochemistry 51(1), 253-290, 2002.
63. R.L. Reuben, J.A. Steel, M. Shehadeh, "Acoustic Emission Source Location for Steel Pipe and Pipeline Applications: The Role of Arrival Time Estimation", Proceedings of the Institution of Mechanical Engineers, Part E: Journal of Process Mechanical Engineering 220(2), 121-133, 2006.
64. A. Mostafapour, S. Davoodi, "Continuous leakage location in noisy environment using modal and wavelet analysis with one AE sensor", Ultrasonics 62, 305-311, 2015.
65. J.G.M. D. GUEORGUIEV, P. DUPONT, L.B. FELSEN, "ANALYSIS OF FLOQUET WAVE GENERATION AND PROPAGATION IN A PLATE WITH MULTIPLE ARRAYS OF LINE ATTACHMENTS", J Sound Vib 234(5), 819-840,
66. P.F.J. M.J. Brennan, J.M. Muggleton and Y. Gao, "On the use of Acoustic Methods to Detect Water Leaks in Buried Water Pipes", 2000.
67. H. Xiao, Butlin, Mark, Tan, Isabella, Avolio, Alberto, "Effects of cardiac timing and peripheral resistance on measurement of pulse wave velocity for assessment of arterial stiffness", Sci Rep-Uk 7(1), 2017.
68. N.D.a.J.F. Maninder Pal, "Detecting & Locating Leaks in Water Distribution Polyethylene Pipes", Proceedings of the World Congress on Engineerin II, 2010.
69. S.I. Raul IONEL, Pavol BAUER, "water leakage monitoring education: cross correlation study via spectral whitening",
70. A.W. Osama Hunaidi, "Acoustic methods for locating leaks in municipal water pipe networks", International Conference on Water Demand Management,
71. W.F. Welsh, "On the Reliability of Cross Correlation Function Lag Determinations in Active Galactic Nuclei", Publ Astron Soc Pac 111, 1999.
72. E.-S.E.-D.a.A.K.G. Ashraf H. Yahia, "Time Delay Estimation Using Correlation Approaches Applied to Seismic Time Picking", 6th International Conference of Applied Geophysics, 2011.
73. O. Hunaidi, W.T. Chu, "Acoustical characteristics of leak signals in plastic water distribution pipes", Appl Acoust 58(3), 235-254, 1999.

74. Y. Xu, V.M. McClelland, Z. Cvetkovic, K.R. Mills, "Coherence and Time Delay Estimation", IEEE Trans Biomed Eng 64(3), 588-600, 2017.
75. M. Pal, "Leak detection and location in polyethylene pipes", Diss. © Maninder Pal, 2008.
76. M.J.B. Y. Gao, and P. F. Joseph, "Time delay estimation of acoustic signals for leak detection in buried plastic pipes", Eleventh international congress on sound and vibration, 3113-3120, 2004.
77. D.R.G. Sumit Kumar, "Estimating time delay using GCC for speech source localisation", International Journal of Application or Innovation in Engineering & Management (IJAIEM) 2(5), 2013.
78. X. Ouyang, L. Luo, J. Xiong, "Time Delay Estimation Using Windowed Differential agnitude of Cross Correlation and Its Hilbert Transform", Procedia Engineering 29, 2033-2038, 2012.
79. K.B.a.P.K. S. R. Mahadeva Prasanna, "Time-Delay Estimation Using Source and Spectral Information from Speech", 2009.
80. A.W.H. Zhang Y, "A comparative study of time-delay estimation techniques using microphone arrays", Department of Electrical and Computer Engineering, The University of Auckland, School of Engineering Report, 2005.
81. D.K.P.a.W.L. Anantha Alifia Putri, "PERFORMANCE COMPARISON BETWEEN GENERALIZED CROSSCORRELATION TIME DELAY ESTIMATION AND FINGERPRINTING METHOD FOR ACOUSTIC EVENT LOCALIZATION", ARPN Journal of Engineering and Applied Sciences 13(13), 4173-4180, 2008.
82. S. Atmadja, Implementation of a Source Tracking system using Cross Correlation of speech signals, 2002.
83. O. Hunaidi, A. Wang, "A new system for locating leaks in urban water distribution pipes", Management of Environmental Quality: An International Journal 17(4), 450-466, 2006.
84. P. Stajanca, S. Chruscicki, T. Homann, et al., "Detection of Leak-Induced Pipeline Vibrations Using Fiber-Optic Distributed Acoustic Sensing", Sensors (Basel) 18(9), 2018.
85. Y. Gao, M.J. Brennan, P.F. Joseph, J.M. Muggleton, O. Hunaidi, "A model of the correlation function of leak noise in buried plastic pipes", J Sound Vib 277(1-2), 133-148, 2004.
86. D.O. Thompson, D.E. Chimenti, Review of progress in quantitative nondestructive evaluation, Springer Science & Business Media2012.
87. O.T.C. Hunaidi, W & Wang, A & Guan, W, "Leak detection methods for plastic water distribution pipes", 1999.
88. Q. Xiao, J. Li, J. Sun, H. Feng, S. Jin, "Natural-gas pipeline leak location using variational mode decomposition analysis and cross-time–frequency spectrum", Measurement 124, 163-172, 2018.
89. Z. Iqbal, M.N. Naeem, N. Sultana, S.H. Arshad, A.G. Shah, "Vibration characteristics of FGM circular cylindrical shells filled with fluid using wave propagation approach", Applied Mathematics and Mechanics 30(11), 1393-1404, 2009.
90. Y.W. Shuaiyong Li, "Modal analysis of leakage-induced acoustic vibrations in different directions for leak detection and location in fluid-filled pipelines", IEEE International Ultrasonics Symposium Proceedings, 2014.
91. R.J.L. Barshinger J N, "Guided wave propagation in an elastic hollow cylinder coated with a viscoelastic material", IEEE transactions on ultrasonics, ferroelectrics, and frequency control 51(11), 1547-1556, 2004.

92. P.K. Kankar, S.C. Sharma, S.P. Harsha, "Rolling element bearing fault diagnosis using wavelet transform", Neurocomputing 74(10), 1638-1645, 2011.
93. N.E. Huang, Z. Shen, S.R. Long, et al., "The empirical mode decomposition and the Hilbert spectrum for nonlinear and non-stationary time series analysis", Proceedings of the Royal Society of London. Series A: Mathematical, Physical and Engineering Sciences 454(1971), 903-995, 1998.
94. P.J.K. A.O. Andrade, S. Nasuto, "Time–frequency analysis of surface electromyographic signals via Hilbert spectrum", in: S.H. Roy, P. Bonato, J. Meyer (Eds.), XVth ISEK Congress—An Invitation to Innovation, Boston, MA, USA, (2004), p. 68.,
95. A.O. Andrade, P.J. Kyberd, S.D. Taffler, A novel spectral representation of electromyographic signals, Proceedings of the 25th Annual International Conference of the IEEE Engineering in Medicine and Biology Society (IEEE Cat. No. 03CH37439), IEEE, 2003, pp. 2598-2601.
96. D.L. Donoho, "De-noising by soft-thresholding", IEEE Trans. Inf. Theory 41(3), 613–627, 1995.
97. J. Choi, J. Shin, C. Song, S. Han, D.I. Park, "Leak Detection and Location of Water Pipes Using Vibration Sensors and Modified ML Prefilter", Sensors (Basel) 17(9), 2017.
98. C.H.K.a.G.C. Carter, "The generalized correlation method for estimation of time delay", Ieee Transactions on Acoustics Speech and Signal Processing Assp-24, No.4, 320-327, 1976.
99. Y. Gao, M.J. Brennan, P.F. Joseph, J.M. Muggleton, O. Hunaidi, "On the selection of acoustic/vibration sensors for leak detection in plastic water pipes", J Sound Vib 283(3-5), 927-941, 2005.
100. Y. Gao, M.J. Brennan, P.F. Joseph, "A comparison of time delay estimators for the detection of leak noise signals in plastic water distribution pipes", J Sound Vib 292(3-5), 552-570, 2006.
101. J. Hur, S. Kim, H. Kim, "Water hammer analysis that uses the impulse response method for a reservoir-pump pipeline system", J Mech Sci Technol 31(10), 4833-4840, 2017.
102. E.S.Gopi, "Algorithm collections for digital signal processing applications using Matlab", 2010.